JM PAPERS

Analyses of Reynolds and Mach number effects on Tollmien–Schlichting wave–bump interaction in subsonic flows

Fernando H.T. Himeno[1],†, A.E.B. Carvalho[1] and M.A.F. Medeiros[1]

[1]Department of Aeronautical Engineering, University of Sao Paulo, Sao Carlos, SP, 13566-590, Brazil

We investigated the effects of two-dimensional sharp-edged rectangular bumps on Tollmien–Schlichting (TS) wave evolution using direct numerical simulation. The bump height, h, ranged from 5 % to 40 % of the local displacement thickness, δ^*. Behind the bump, a recirculating flow region could be formed whose length increased nonlinearly with h. The bump height effect on the TS wave, which was the dominant, scaled super-exponentially with h. We also showed a substantial effect of the δ^*-based Reynolds number, $Re_{\delta*}$. Firstly, the bump wake extended with $Re_{\delta*}$, promoting larger TS wave growth rates. The second effect is related to proximity to the upper branch of the instability loop, accounting for the influence of the TS frequency, as well. It dictates the bump impact increases as it gets closer to transition, either by the bump moving downstream or the transition moving upstream. For a 40 % high bump, for example, changing the $Re_{\delta*}$ at the bump location from 1500 to 2000 increased ΔN by a factor of 2 (ΔN represents a measure of a surface irregularity effect on the smooth plate N-factor). We also found that $(\Delta N)_{max}$ increases linearly with Re_{hh}. Results in the subsonic regime showed that the bump impact attenuates with Mach number up to 0.7 but above it, stabilisation is surpassed by the destabilising effect caused by the recirculation lengthening. This is mostly associated with the bump wake that extends with the pressure gradient which increases substantially towards the sonic speed. This is enhanced if the surface is adiabatic rather than isothermal.

Key words: boundary layer stability, transition to turbulence, compressible boundary layers

1. Introduction

It is estimated that the profile component is responsible for approximately 50 % of the total drag of a commercial aircraft (Marec 2001). Several efforts have been conducted to develop strategies to delay the turbulent regime; hence, a better understanding of boundary

† Email address for correspondence: fernando.himeno@gmail.com

layer transition phenomena is desirable. The transition point depends on, for example, the so-called Tollmien–Schlichting (TS) waves. These waves can be amplified along the boundary layer, eventually leading to turbulence (Morkovin 1969; Reshotko 1976; Kachanov 1994; Saric, Reed & Kerschen 2002). This scenario becomes more complex in a practical situation because surfaces are not perfectly smooth. The interaction with a two-dimensional bump affects the amplitude of the TS waves in comparison with a smooth surface (Wörner, Rist & Wagner 2003; Sumariva, Hein & Valero 2020). This is the focus of the current investigation.

Some criteria for the critical height of surface imperfections were initially proposed by earlier experimental studies (Tani, Hama & Mituisi 1940; Fage & Preston 1941; Dryden 1953; Carmichael 1959; Tani 1961). These criteria, however, were based on semi-empirical formulas limited to specific conditions. In experiments with circular-section wires, Klebanoff & Tidstrom (1972) provide a more detailed discussion concerning the physical mechanism by which the transition is affected by bumps. They show that the bump enhances the amplification of the already existing TS waves as they travel along the unstable region just downstream of the bump, the so-called recovery zone. At the end of this region, the evolution returns to that of the smooth surface one.

In some early theoretical studies (Nayfeh, Ragab & Al-Maaitah 1988; Masad & Iyer 1994), the base flows were obtained by the interacting boundary layer (IBL) method, which restricted the study to smooth-shaped bumps. Later, the triple-deck theory was used to investigate the effect of surface imperfections in the presence of separated flows (Mengaldo *et al.* 2015). For more critical shapes, such as those containing corners, one must use a more complex and, consequently, more computationally demanding method to handle the higher gradients caused by the corners. Recently, the so-called harmonic linear Navier–Stokes (HLNS) and the adaptive HLNS methods have been used to investigate the effect of sharp-edged steps and bumps (Hildebrand, Choudhari & Paredes 2020; Sumariva *et al.* 2020). The impact of the bump height is far more critical than its length (Wörner *et al.* 2003). This is particularly noticeable for the sharp-edged bumps as shown by Sumariva *et al.* (2020). These studies also show that, compared with other shapes, the sharp-edged element is the most critical. This was noticed earlier by Obara & Holmes (1986). Rectangular bumps are also more relevant in the context of receptivity (Raposo, Mughal & Ashworth 2018; Placidi, Gaster & Atkin 2020; dos Santos *et al.* 2024).

The influence of two-dimensional bumps on transition has been investigated in parallel with forward- (FFS) and backward-facing step (BFS) studies (Dovgal & Kozlov 1990; Wang & Gaster 2005; Crouch & Kosorygin 2020). The e^N method proposed van Ingen (1956) and Smith & Gamberoni (1956) has been widely used to estimate the effect of imperfections on the evolution of TS waves (Nayfeh *et al.* 1988; Cebeci & Egan 1989; Crouch, Kosorygin & Ng 2006; Crouch & Kosorygin 2020). The amplification factor for some individual frequency (here denoted as the *n*-factor) is given by $n(x) = \ln(A_{TS}(x)/A_{TS,0})$, where $A_{TS}(x)$ represents the evolution of the TS wave amplitude and $A_{TS,0}$ is the TS wave amplitude at the lower branch of the stability diagram. The parameter $N(x)$ is used to refer to the envelope curve considering the *n*-factor curves of all TS waves, $N(x) = \max_{TS}\{n_{TS}(x)\}$. In the e^N method, the transition is predicted to occur for the TS wave whose *n*-factor first exceeds some critical value, N_{cr}.

Despite being still dependent on the value of N_{cr} determined empirically, in comparison with the earlier correlation formulas (Fage & Preston 1941; Carmichael 1959), the e^N method is much more precise since it accounts for aspects such as the turbulence intensity. In this framework, the change on transition location caused by some imperfection has been estimated by evaluating its impact as a jump on the *N*-factor curve, ΔN. The impact

of different flow conditions and surface imperfections becomes directly represented by the resulting ΔN that each case presents. Experimental and numerical studies on this topic base their analysis on the change of N-factor (Wang & Gaster 2005; Crouch & Kosorygin 2020; Hildebrand *et al.* 2020; Sumariva *et al.* 2020). Wang & Gaster (2005) showed experimentally that the BFS has a stronger impact compared with the FFS. Similar results are presented by Crouch & Kosorygin (2020), which also shows that the effect on ΔN caused by a bump (tape) is consistent with the idea that it is composed of the sum of the independent impacts of an FFS and a BFS.

In this paper, we investigate the influence of three parameters that are usually neglected in the current use of ΔN when accounting for the impact of two-dimensional bumps. We show that, under some circumstances, some of these assumptions can lead to substantial inaccuracy in transition predictions. The first is that it is often considered that the frequency of the TS wave leading to transition is not affected by the bump. However, earlier theoretical results from Nayfeh *et al.* (1988) show that the frequency of the dominant TS wave shifts towards higher frequencies compared with the smooth plate as the bump height increases. Masad & Iyer (1994) present the same conclusions, and Klebanoff & Tidstrom (1972) also observed this effect in their experiments.

The second aspect concerns the effect of the Reynolds number at the bump location. In the more recently obtained correlations for ΔN as a function of a two-dimensional roughness height, the results are grouped regardless of the Reynolds number, but a closer look reveals that there are trends that could be assigned to the Reynolds number. Klebanoff & Tidstrom (1972) showed that, for a given bump height relative to the displacement thickness (δ^*), the impact of the bump increases with the Reynolds number, but this effect is not as important as that of increasing height. Nayfeh *et al.* (1988) found that the impact of a bump with fixed dimensional height decreases as it is placed progressively downstream. However, since, in this situation, the bump height relative to the local boundary layer thickness reduces as it is placed downstream, the effect of height may be offsetting the effect of the Reynolds number. Masad & Iyer (1994) also investigated the effect of the Reynolds number for two-dimensional bumps, but once again, the exclusive effect of the Reynolds number could not be extracted from the results. Nevertheless, there were a couple of examples that correspond to cases with virtually the same height relative to δ^* for two different Reynolds numbers. The results indicated the impact of the bump increased with Reynolds number. Crouch & Kosorygin (2020) also observed some effect of Reynolds number for FFS that they also noticed in Wang & Gaster (2005). For the bump and BFS cases, however, they did not find similar behaviour. For the bump, they even noticed some reduced impact as it was moved downstream. In any case, owing to the form in which the data are presented, it is difficult to extract information about the Reynolds number effect on each of these studies. In this paper, we will present results of the effect Reynolds number in conditions where other parameters are kept fixed, in particular, the bump height relative to the local δ^*.

A third aspect somewhat overlooked in the recent literature is the effect of compressibility in the transonic regime. It is known that compressibility stabilises the TS waves (Schlichting & Gersten 2000). On the other hand, compressibility extends the recirculating flow behind the bumps, which has a destabilising effect on TS waves, as shown in Masad & Iyer (1994). Considering both effects, they found a stabilising net impact up to $M_\infty = 0.8$. When investigating the effect of BFS, Nayfeh (1992) also found similar contrasting effects of compressibility. Far downstream, however, they noticed that the N-factors were virtually independent of the Mach number. More recently, Costantini, Risius & Klein (2022) found that, for the FFS, the compressibility had a small effect

on transition. For waviness, Wie & Malik (1998) and Perraud *et al.* (2004) also report these opposing effects. Wie & Malik (1998) suggest for long wavelength waviness that the destabilising effect could offset the stabilising one as the free-stream Mach number (M_∞) increases. In any case, all these results from the literature in the subsonic regime are limited to $M_\infty = 0.8$.

Here, we employed direct numerical simulation (DNS), an approach already adopted in investigations of sharp-edged bumps in incompressible flow (Wörner *et al.* 2003). However, to represent the bump, Wörner *et al.* employed an immersed boundary technique, which meant that some degree of smoothness was present on the bump corners. In the present study, we use an in-house compressible DNS that allows the inclusion of cavities or bumps with sharp corner edges aligned with a Cartesian grid. Studies on topics related to flow instability that were conducted with the present code can be found in Martinez & Medeiros (2016), Mathias & Medeiros (2018), Himeno, Mathias & Medeiros (2021), Mathias & Medeiros (2021) and Himeno, Carvalho & Medeiros (2023).

Studies of the effect of roughness on transition often use the Reynolds numbers, Re_{hh}, sometimes also referred to as Re_{kk}. This Reynolds number is defined as $Re_{hh} = u_h^\star h^\star/\nu^\star$, where the $\star$ denotes dimensional value, $h^\star$ is the bump height, $u_h^\star$ denotes the smooth case streamwise velocity evaluated at the bump top and $\nu^\star$, the fluid viscosity. It is often considered that a surface is hydraulically smooth for $Re_{hh} < 25$ (Morkovin 1990). This represents a bound below which an isolated roughness does not affect transition. The most critical condition is that in which transition occurs at the roughness element. For this condition, Dryden (1953) estimates a Reynolds number of $Re_{hh} = 169$ for a cylindrical roughness element (a wire) while Tani (1961) shows that it varies in the range 150 to 300. Tani (1961) also shows that such maximum impact does not occur at the bump itself but slightly downstream of the bump. The bumps we simulated are in the range of Re_{hh} from 1.4 to 184. Also sometimes used is $Re_h = U_\infty^\star h^\star/\nu^\star$ (also called Re_k), $U_\infty^\star$ being the free-stream velocity. In our study, Re_h ranges from 47.5 to 800. Here, we show the bump causes a maximum ΔN-factor that occurs at some distance downstream of the bump, consistently with the Tani (1961) results. We also found that the maximum ΔN caused by the sharp-edged rectangular bumps scales almost linearly with Re_{hh}. The same holds for the length of the recirculating flow behind the bump. This suggests that the maximum ΔN impact that a bump exerts is associated with the recirculating flow in its wake.

Our study confirmed both the important effects of bump height and the dominant TS wave upward frequency shift. The bump deforms the base flow. For small bumps, the growth rate deviation from the smooth case scales linearly with bump height. This leads to an exponential effect on the TS wave amplitude deviation from the smooth case. For higher bumps, the growth rate deviation scales quadratically with bump height, with a super-exponential impact on the TS wave amplitude. Regarding the influence of the Reynolds number, our results showed that, for a fixed bump height relative to δ^*, a Reynolds number increase promotes an earlier transition because it extends the region of recirculating flow behind the bump. We also found that the TS wave–bump interaction becomes more critical as the bump approaches the upper branch of the instability diagram. We collected results from the literature of Klebanoff & Tidstrom (1972) and Masad & Iyer (1994) and placed the bump and transition location of their test cases on the smooth stability diagram. This plot confirmed what we refer to as the upper branch effect. This phenomenon amounts to an influence of frequency on the TS wave–bump interaction and to another destabilising effect of the Reynolds number. It also amounts to an influence of TS amplitude on the effective ΔN, an issue often overlooked in the literature. Upon investigating the influence of compressibility, we found a stabilising effect up to

$M_\infty = 0.7$. Above it, however, we found an overall destabilising effect. This is associated with the fact that compressibility increases the pressure gradients produced by the bump and, as a consequence, increases the bump wake separation region. We draw some conjectures that suggest a strong destabilising effect in the transonic regime. Considering an adiabatic wall enhances the destabilising effect of the bump.

The paper is organised as follows. Next, we present the methods used. Following that, we assess the accuracy of our computational results. The elementary effects of a bump on a TS wave evolution are presented in § 4. The influence of Reynolds number on the base flow is addressed in § 5. Section 6 presents the effects of Reynolds number and TS wave frequency on the TS wave–bump interaction. The combined effects of the bump height and local Reynolds number are addressed in § 7. The influence of compressibility is discussed in § 8. Final remarks and conclusions are given in § 9.

2. Methods

2.1. *Governing equations*

The in-house DNS code solves the complete set of conservation equations that governs three-dimensional compressible flows. These equations can be written in non-conservative, non-dimensional form as

$$\frac{\partial \varrho}{\partial t} = -\varrho \frac{\partial u_i}{\partial x_i} - \frac{\partial \varrho}{\partial x_i} u_i, \tag{2.1}$$

$$\frac{\partial u_j}{\partial t} = -\frac{\partial u_j}{\partial x_i} u_i - \frac{1}{\varrho} \frac{\partial p}{\partial x_j} + \frac{1}{\varrho} \frac{\partial \tau_{ij}}{\partial x_i}, \tag{2.2}$$

$$\frac{\partial e}{\partial t} = -\frac{\partial e}{\partial x_i} u_i - \frac{p}{\varrho} \frac{\partial u_i}{\partial x_i} + \frac{1}{\varrho} \tau_{ij} \frac{\partial u_i}{\partial x_i} - \frac{1}{\varrho} \frac{\partial q_i}{\partial x_i}, \tag{2.3}$$

with u_i ($i = 1, 2, 3$) denoting the velocity components along the three Cartesian directions. In the current study, the simulations were restricted to two dimensions: streamwise (x) and wall-normal directions (y). Here, ϱ, e and p denote density, internal energy and pressure, respectively. The viscous tensor, τ_{ij}, and the heat flux, q_i, are defined as

$$\tau_{ij} = \frac{\mu}{Re} \left(\frac{\partial u_i}{\partial x_j} + \frac{\partial u_j}{\partial x_i} - \frac{2}{3} \delta_{ij} \frac{\partial u_k}{\partial x_k} \right), \quad q_i = -\frac{\mu}{(\gamma - 1)Re\,Pr\,M_\infty^2} \frac{\partial T}{\partial x_i}, \tag{2.4a,b}$$

where *Re*, *Pr* and M_∞ represent the Reynolds, Prandtl and Mach numbers, respectively. The subscript ∞ indicates free stream and δ_{ij} is the Kronecker delta function ($\delta_{ij} = 0$, if $i \neq j$; $\delta_{ij} = 1$, if $i = j$). Also, γ indicates the fluid heat capacity ratio, μ the dynamic viscosity and T the temperature. Variables are non-dimensionalised by the dimensional (superscripts $\star$) values of the Blasius displacement thickness ($\delta_{x_R}^{*}{}^{\star}$) at the centre of the bump ($x_R^{\star}$) and by the free-stream velocity ($U_\infty^{\star}$), density ($\varrho_\infty^{\star}$) and temperature ($T_\infty^{\star}$). The simulation Reynolds number is defined as $Re = Re_{\delta^*} = \varrho_\infty^{\star} U_\infty^{\star} \delta_{x_R}^{*}{}^{\star} / \mu_\infty^{\star}$. The Prandtl number is defined as $Pr = \mu_\infty^{\star} c_p^{\star} / k^{\star}$, where $c_p^{\star}$ and $k^{\star}$ denote the fluid specific heat and thermal conductivity, respectively. The Mach number is defined as

Scheme	Nodes	α	a	b	c	d
SL6-O-Sym.	$4 \leq i \leq (M-3)$	0.392465753	1.565410959	0.237260274	-0.017739726	0
SL4-O-Sym.	$i = \{3, M-2\}$	0.350978474	1.567318982	0.134637965	0	0
C4-Sym.	$i = \{2, M-1\}$	1/4	3/2	0	0	0
C3-O-Asym.	$i = 1$	2.836465295	-2.778821765	1.581767352	1.336465295	-0.139410882
C3-O-Asym.	$i = M$	2.836465295	2.778821765	-1.581767352	-1.336465295	0.139410882

Table 1. Derivative scheme coefficients. The scheme is identified as 'SL' (spectral-like) or 'C' (compact), followed by its order of accuracy, 'O' (if optimised) and, finally, by 'Sym.' (symmetric) or 'Asym.' (asymmetric).

$M_\infty = U_\infty^\star / \sqrt{\gamma p_\infty^\star / \rho_\infty^\star}$. Non-dimensional variables are, hence, calculated as

$$\left. \begin{aligned} \varrho = \frac{\varrho^\star}{\varrho_\infty^\star}, \quad p = \frac{p^\star}{\varrho_\infty^\star U_\infty^{\star 2}}, \quad x_i = \frac{x_i^\star}{\delta_{x_R}^{* \star}}, \quad T = \frac{T^\star}{T_\infty^\star}, \quad u_i = \frac{u_i^\star}{U_\infty^\star}, \\ t = \frac{t^\star U_\infty^\star}{\delta_{x_R}^{* \star}}, \quad e = \frac{e^\star}{U_\infty^{\star 2}}. \end{aligned} \right\} \tag{2.5a--g}$$

The fluid is considered an ideal gas, and the viscosity is modelled by Sutherland's law: $\mu = ((1 + C)/(T + C)) \, T^{3/2}$, with $C = (110 \text{ K})/T_\infty^\star$. For all simulations presented here, $Pr = 0.71$, $\gamma = 1.4$ and $T_\infty^\star = 300 \text{ K}$.

2.2. *Numerical methods*

The spatial derivatives are calculated by a finite-difference-spectral-like scheme (Lele 1992). Consider some generic variable, $\phi(x)$, discretised along x with M nodes ($i = 1, 2, \ldots, M$). The first derivative, $\phi'(x)$, at some node far from the boundaries, can be approximated by the following symmetric formula:

$$\alpha \phi_{i-1}' + \phi_i' + \alpha \phi_{i+1}' = a \frac{\phi_{i+1} - \phi_{i-1}}{2\Delta} + b \frac{\phi_{i+2} - \phi_{i-2}}{4\Delta} + c \frac{\phi_{i+3} - \phi_{i-3}}{6\Delta}, \tag{2.6}$$

where α, a, b and c are adjustable coefficients and Δ is the mesh spacing. For boundary nodes ($i = 1$ or M), the scheme must be asymmetric and the formula becomes

$$\phi_{1,M}' + \alpha \phi_{2,M-1}' = a \frac{\phi_{1,M}}{\Delta} + b \frac{\phi_{2,M-1}}{\Delta} + c \frac{\phi_{3,M-2}}{\Delta} + d \frac{\phi_{4,M-3}}{\Delta}. \tag{2.7}$$

In our implementation, the algebraic system is tridiagonal. The coefficients were optimised for the current application by setting constraints based on the integral of the dispersive error, a strategy proposed by Gaitonde & Shang (1996). Table 1 shows the coefficients of the derivative scheme that we used in our simulations. Except for the boundary nodes, the derivative scheme is made symmetric by reducing the stencil size and lowering its order compared with the central domain scheme (Silva, Souza & Medeiros 2010). This reduces dispersive errors related to asymmetric schemes (Gaitonde & Visbal 1998).

For the time integration, the classic fourth-order Runge–Kutta scheme was employed. The code is written in Fortran 90 and the parallelisation is made by the *pencil* or *slab* approach (Li & Laizet 2010). The code is available on GitHub (https://github.com/
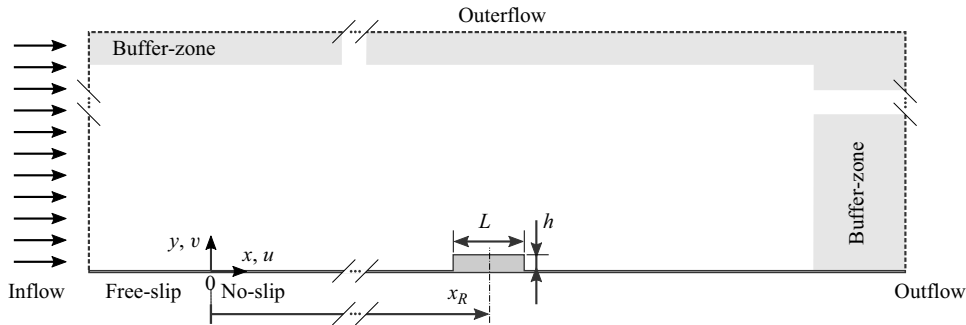
Figure 1. Schematic of the computational domain with a flat plate containing a bump.

marlonsmathias/GATT_DNS). Further details of the DNS code development and use can be found in Bergamo *et al.* (2015), Martinez & Medeiros (2016), Mathias & Medeiros (2018), Himeno *et al.* (2021), Mathias & Medeiros (2021) and Himeno *et al.* (2023).

The DNS code was developed to simulate the boundary layer on a flat plate on which rectangular elements aligned with the grid can be placed. The grid is Cartesian and can be stretched along any direction. Figure 1 presents a schematic domain of the flat plate containing a rectangular bump located at x_R with length, $L = L^\star/\delta_{x_R}^{* \star}$, and height, $h = h^\star/\delta_{x_R}^{* \star}$.

Buffer zones separate the physical domain from the outflow and outer flow boundaries to avoid any contamination from spurious reflections. Along the buffer region, the amplitude of disturbances is smoothly dissipated by increasing the grid size, changing the derivative scheme to lower-order explicit schemes and also, by applying a low-pass temporal filter, the selective frequency damping proposed by Åkervik *et al.* (2006).

A spatial low-pass filter is employed to avoid the aliasing effects due to mesh discretisation. The code is implemented with the tridiagonal tenth-order scheme proposed by Gaitonde & Visbal (1998). It depends only on the parameter α_f that can assume a value between -0.5 (maximum filtering) and 0.5 (no filtering). In the current simulations, we set $\alpha_f = 0.49$, which means that the spatial filter was very weak. Moreover, it was only applied far from the boundaries, hence, near to the wall, the solution was not filtered.

The boundary conditions used were:

(i) Inflow: $[u, v, T] = [U_\infty, 0, T_\infty]$ and $\partial p/\partial x = 0$.
(ii) Outflow: $(\partial^2/\partial x^2)[u, v, T] = [0, 0, 0]$ and $p = p_\infty$.
(iii) Outer flow: $(\partial^2/\partial y^2)[u, v, T, p] = [0, 0, 0, 0]$.
(iv) Walls: $\partial p/\partial \boldsymbol{n} = 0$, where $\boldsymbol{n}$ denotes the normal-to-wall direction. At the corner nodes, the pressure is set as the mean value that meets the boundary condition for each direction. This has a small influence on the results as both values come very close to each other and using either value leads to essentially the same solution. We employ the mean to avoid bias. We also used effectively identical grid spacing at the corner in both y and x direction to further minimise possible errors. For temperature, we take $T = T_\infty$ if the wall is assumed isothermal, or $\partial T/\partial \boldsymbol{n} = 0$ if adiabatic. For the velocity components:
   (*a*) for $x \geq 0$ (no-slip region): $[u, v] = [0, 0]$;
   (*b*) for $x < 0$ (free-slip region): $v = 0$, $\partial u/\partial y = 0$. The free-slip condition is used along the wall between the inflow and the plate leading edge ($x < 0$) (Mathias & Medeiros 2018, 2021). This reduces the suction peak at the leading edge and

provides a more uniform pressure along the plate. The length of this region controls the magnitude of the suction peak. In the study, we ensured that the numerical solution was very close to the theoretical Blasius profile at the excitation region and beyond. In our simulations, in this region, the profile was indistinguishable from the Blasius one and was less than 0.3 % thicker.

2.3. *Flow disturbance*

In our approach, a controlled excitation disturbance is introduced by imposing a non-null velocity at the wall. For the monochromatic cases, the wall-normal component was used (blow/suction condition). The disturbance is located at $x = x_D$ and covers a length of L_D, with the excitation function defined as

$$v(x, t)|_{wall} = A_D \sin(\alpha_{TS}x) \sin(\omega t), \quad x = x_D + [-L_D/2; L_D/2], \tag{2.8a,b}$$

where A_D is the magnitude of the velocity component, $\alpha_{TS} = 2\pi/L_D$ and ω is the angular frequency of the TS wave. In our study, A_D was chosen to ensure that the TS wave remained in the linear regime throughout the computational domain. The amplitude was not the same for all tests. The value of α_{TS} is chosen to match approximately the wavelength of the expected TS wave, as this reduces the magnitude of the excitation needed and prevents nonlinear effects at the excitation source. The frequency used for monochromatic TS wave simulations was not the same for all tests, hence α_{TS} also varied. As a consequence, the suction and blowing slot width, L_D, which depends on α_{TS}, was not the same for all simulations. In our study, the monochromatic disturbance was used for the mesh independence (§ 3.1) and in the validation tests (§ 3.3). Both A_D and L_D are specified in the sections concerned.

   We also used a wave packet excitation, meant to produce a flat spectrum with no bias to any frequency within the frequency range of interest. This is best achieved by defining the signal as a flat spectrum in the frequency band of interest and converting this signal to physical space (Medeiros & Gaster 1999*a,b*). For the wave packet disturbance, the streamwise-velocity component was used (slipping condition) instead of the wall-normal one. Compared with the blow/suction condition, the slipping wall produces an acoustic dipole rather than a monopole, which is less efficient in producing the unwanted acoustic waves that arise as the flow is excited. The wave packet disturbance excitation took the form

$$\left.\begin{array}{c} u(x, t)|_{wall} = \displaystyle\sum_{k=1}^{n_k} A_0 \mathsf{G}_t \mathsf{G}_x \cos(k\omega_0 t), \\[12pt] \mathsf{G}_t = \exp\left(-\dfrac{\left(t - \dfrac{1}{8}\dfrac{2\pi}{\omega_0}\right)^2}{2\left(\dfrac{1}{16}\dfrac{2\pi}{\omega_0}\right)^2}\right), \quad \mathsf{G}_x = \exp\left(-\dfrac{(x - x_D)^2}{2(L_D/8)^2}\right), \\[20pt] x = x_D + \left[-\dfrac{L_D}{2}; \dfrac{L_D}{2}\right], \quad t = \left[0, \dfrac{1}{4}\dfrac{2\pi}{\omega_0}\right], \end{array}\right\} \tag{2.9}$$

where ω_0 is the lowest-frequency component and n_k is the number of modes considered. Along the x-direction, the function ends are made smooth by using a Gaussian function G_x. To reduce the excitation time and hence the total simulation time, another Gaussian function (G_t) was used to smoothly cut the excitation time interval. Figure 2(*a,b*) shows
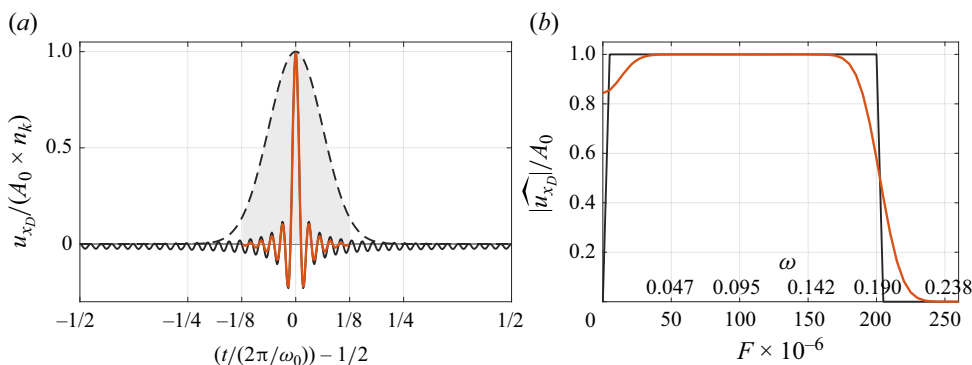
Figure 2. Comparison of the modified wave packet excitation disturbance function used in simulations of cases with $Re_{\delta*} = 950$ and $M_\infty = 0.1$ (solid red) and the original wave packet function (solid black). (*a*) Physical space and (*b*) the corresponding spectral content. The packet is composed of the sum of $n_k = 40$ modes of the fundamental frequency $F_0 = 5 \times 10^{-6}$, all with the same amplitude, $A_0 = 1.04 \times 10^{-4}$ (see table 2).

$Re_{\delta*}$	$F_0\ (\omega_0)$	A_0	n_k
950	5.0×10^{-6} (0.0048)	1.04×10^{-4}	40
1500	2.5×10^{-6} (0.0037)	1.00×10^{-5}	80
2000	2.5×10^{-6} (0.0050)	1.00×10^{-5}	80

Table 2. Parameters of the wave packet excitation disturbance used in simulations with $M_\infty = 0.1$ for the bumps located at different $Re_{\delta*}$.

the physical and spectral content of the original wave packet and the wave packet modified by the Gaussian envelope. The time interval needed to include the packet is reduced to a quarter of that of the original one. The amplitude of low-frequency modes was slightly affected by G_t. However, the function parameters were set to ensure that the modes within this band are sufficiently damped by the boundary layer so as not to influence the analysis.

Figure 2 shows results for simulations in which the bump was centred at $Re_{\delta*} = 950$. For other conditions the results are similar. The parameters of the wave packet excitation in (2.9) are presented in table 2 for all conditions. The reduced frequency is given by $F = \omega^\star v^\star / U_\infty^{\star 2} = \omega / Re_{\delta*}$. The amplitude of the wave packet was chosen roughly as the maximum amplitude that would still ensure the linear regime as addressed in § 3.2. The frequency range was chosen to ensure the most unstable TS waves were excited. This is further addressed and shown in § 6. The frequency discretisation ensured a visually well-defined wave packet in physical and spectral domains.

3. Preparatory computational tests

3.1. *Mesh and domain*

In our study, we investigated bumps with heights as low as 5 % of the local displacement thickness. For the TS wave of $F = 90 \times 10^{-6}$, a 5 % high bump with length $L = 18.2$ centred at $Re_{\delta*} = 950$ ($x_R = 320.8$) can increase the TS wave amplitude by 2.5 % relative to that for the smooth plate. To investigate this effect, a compromise between accuracy and computational cost had to be reached. We considered the results independent of mesh if the maximum variation of amplitude were approximately 0.5 %. For this study, the TS wave was excited by wall suction and blowing. The disturbance was centred at $Re_{\delta*} = 700$
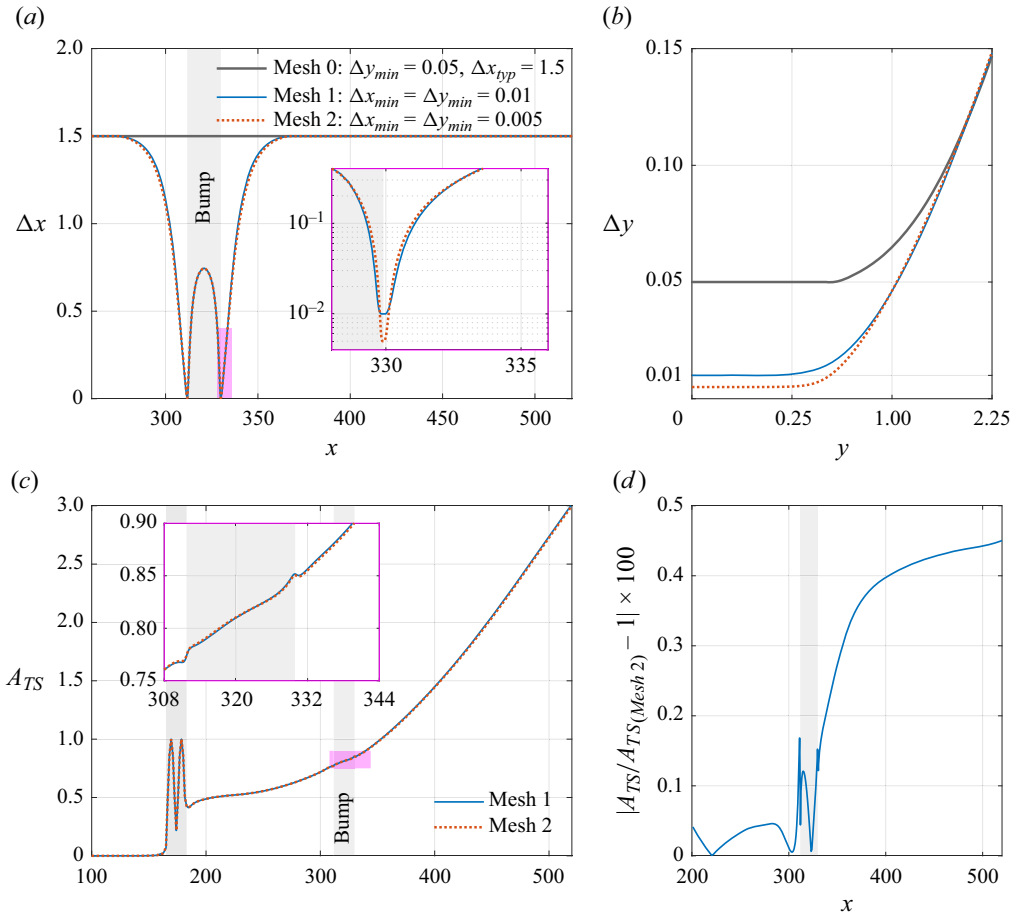
Figure 3. Mesh independence analysis for a TS wave interacting with a $5\% \times \delta^*$ high bump. The bump is located at $x_R = 320.82$ ($Re_{\delta^*} = 950$) and stretches along a length of $L = 18.18$, indicated by the shaded area. The figure shows the mesh properties along (*a*) the *x*-direction and (*b*) the *y*-direction. The plot (*c*) shows the TS amplitude evolution along the plate for each mesh and (*d*) the respective absolute change with respect to the finest grid (mesh 2). Zoomed views are also provided on areas indicated by the magenta boxes. Here, $F = 90 \times 10^{-6}$.

($x_D = 174.0$) and had a slot length of $L_D = 18.0$. The meshes '0' to '2' used in the tests are discussed with the help of figure 3. The properties of all meshes are summarised in table 3. For a smooth plate, the grid requirements are not so severe as shown in our previous study (Himeno *et al.* 2023). The minimum mesh spacing of $\Delta y_{min} = 0.05$ along the *y*-direction is sufficient. The typical mesh spacing in the *x*-direction (Δx_{typ}) is better defined in terms of the number of nodes per TS wavelength. A value of Δx_{typ} corresponding to approximately 13 grid points per TS wavelength is necessary to provide the accuracy required, which led to a value of 1.5. The 'mesh 0' in figure 3(*a,b*) denotes the mesh that produced independent solutions for the smooth case. For a plate containing a bump, the most critical mesh parameter is the refinement at the bump corners. Figure 3(*c*) presents the solutions for a monochromatic TS wave interacting with a 5 % high bump conducted with different levels of refinement at the bump region, indicated in figure 3(*a,b*) as 'mesh 1' and 'mesh 2.' As discussed in § 2.2, Δx_{min} was made equal to Δy_{min} also to diminish errors related to the pressure boundary condition at the corners. As shown by

998 A11-10

	(x_i, x_f)	(y_i, y_f)	Δx_{typ}	Δx_{min}	Δy_{min}	N_x	N_y	Obs.
mesh 0	$(-99.0, 775.0)$	$(0, 26.2)$	1.5	1.5	0.05	474	78	S, M, (§ 3.1)
mesh 1	$(-99.0, 773.6)$	$(0, 26.2)$	1.5	0.01	0.01	686	124	R, M, (§ 3.1)
mesh 2	$(-99.0, 773.6)$	$(0, 26.2)$	1.5	0.005	0.005	710	168	R, M, (§ 3.1)
mesh 3	$(-98.0, 900.0)$	$(0, 21.2)$	2.8	2.8	0.0117	316	138	S, M, (§ 3.3)
mesh 4	$(-98.0, 900.0)$	$(0, 21.2)$	2.8	0.0117	0.0117	538	138	R, M, (§ 3.3)
mesh 5	$(-50.0, 739.5)$	$(0, 29.6)$	1.25	1.25	0.01	516	150	S, W, (§§ 4–8)
mesh 6	$(-50.0, 739.5)$	$(0, 29.6)$	1.25	0.01	0.01	685	150	R, W, (§§ 3.1, and 4–8)
mesh 7	$(-50.0, 818.4)$	$(0, 56.4)$	1.25	0.01	0.01	710	215	R, W, (§ 3.1)
mesh 8	$(-50.0, 1931.4)$	$(0, 29.7)$	1.25	0.01	0.01	1488	161	R, W, (§§ 5–6)
mesh 9	$(-50.0, 1722.7)$	$(0, 29.7)$	1.25	0.01	0.01	1321	161	R, W, (§§ 5–6)

Table 3. Properties of the meshes used in the present simulations. The last column (observations) provides some details of the simulations conducted with each mesh; 'S': smooth plate, 'R': rough plate, 'M': monochromatic disturbance, 'W': wave packet disturbance. The last column also includes the sections the meshes are used in the paper.

the relative amplitude error in figure 3(*d*), the mesh with $\Delta x_{min} = \Delta y_{min} = 0.01$ satisfies the criterion of a relative error around 0.5 %. Despite being a very small grid element, the highest refinement level region is very localised and the mesh is rapidly stretched along both directions up to the refinement necessary to simulate the smooth plate TS wave evolution.

In the validation test section (§ 3.3), we compare our results with those from Wörner *et al.* (2003), who studied the evolution of a TS wave of $F = 49.34 \times 10^{-6}$. For that, meshes '3' and '4' were used. The typical *x* spacing of $\Delta x_{typ} = 2.8$ is consistent with the criterion of 13 grid points per TS wavelength for that parameter space. The minimum grid sizes in the *x*- and *y*-directions are of the order of 0.01. The value of $\Delta x_{min} = \Delta y_{min} = 0.0117$ fits the grid to the authors' roughness height.

In § 4, the simulations were conducted with meshes '5' and '6.' This section employed wave packet simulations. The typical $x-$ grid used was $\Delta x_{typ} = 1.25$ to satisfy the criterion of 13 grid points per TS wavelength for the lowest frequency of interest in the packet.

In §§ 5 and 6, besides meshes '5' and '6', meshes '8' and '9' were used to account for the higher bump-location Reynolds numbers. A corresponding smooth plate mesh was also used. Figure 4 shows every 4 nodes along both the *x*- and *y*-directions. This plot illustrates how the mesh nodes are distributed along the domain relative to the dimensions of the bump of $h = 0.40$ at $Re_{\delta*} = 950$.

Besides the grid refinement, it is also necessary to verify that the results are independent of the computational domain. As will be seen later, this becomes more critical for larger bumps as the Mach number approaches 1. Figure 5 compares the results of mesh '6' and mesh '7' which is twice as long in the vertical direction (see table 3). The figure indicates that mesh '6' is not domain independent as M_∞ and h increase. In the compressibility effect studies (§ 8), mesh '7' was used for simulations with $M_\infty \geq 0.7$ and $h \geq 0.30$. Other than that, mesh '6' was used. Results suggest that simulations with mesh '7' are sufficiently accurate to support the conclusions.

3.2. *Linearity of TS wave and compressibility issues*

A comparison between DNS and linear incompressible parabolised stability equations (PSE) results for the TS wave amplitude evolution along the smooth plate is presented
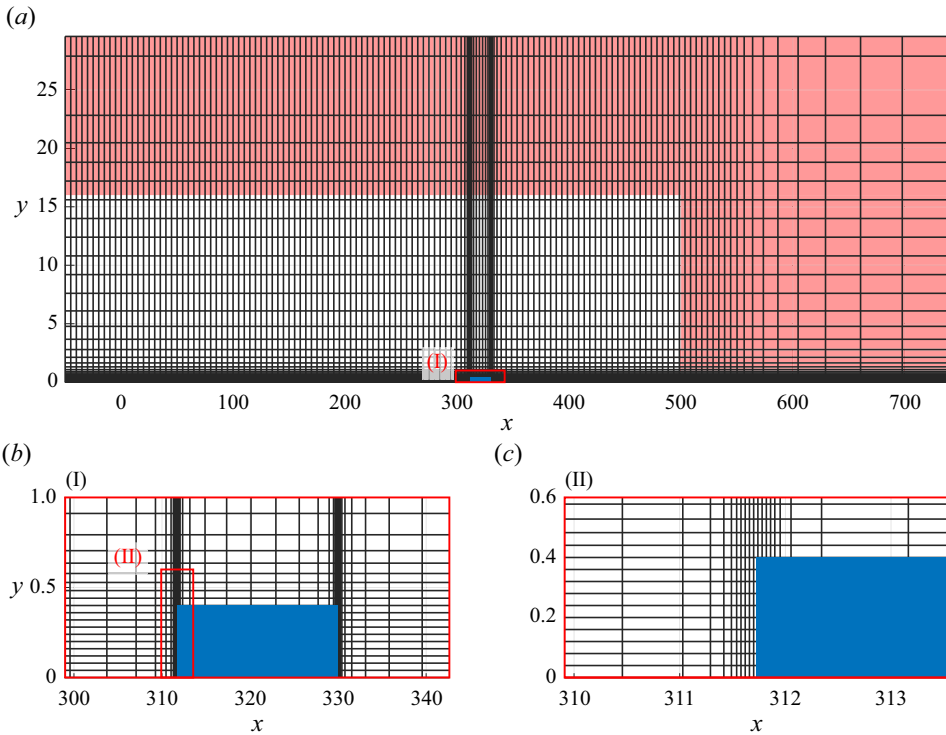
Figure 4. 'Mesh 6' grid showing one every 4 nodes along both directions. A detail is provided for the region (I) containing the bump of $h = 0.40$ at $Re_{\delta*} = 950$ (blue). A detailed view is given of region (II) at the bump leading edge. Buffer zones are indicated by the magenta areas.
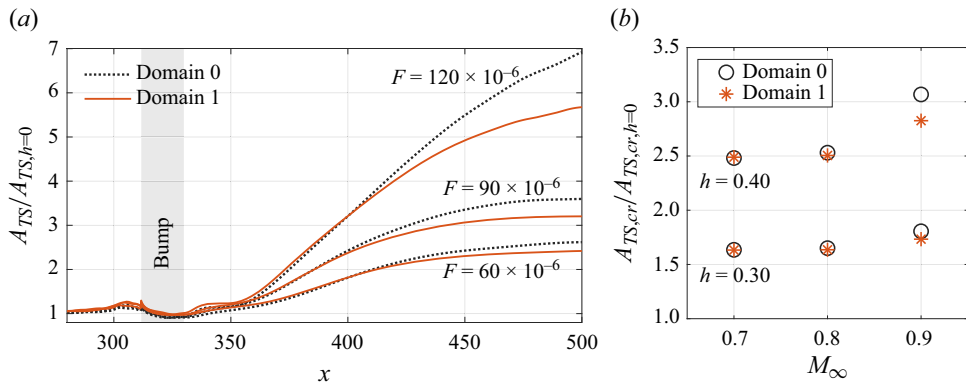

Figure 5. Domain independence analysis. (*a*) Amplitude evolution relative to the smooth plate for the case with a bump of $h = 0.40$ at $Re_{\delta*} = 950$, $M_\infty = 0.90$ and selected frequencies, considering meshes '6' and '7' with different domains. (*b*) The amplitude of the dominant TS wave at $x = 500.0$ relative to the smooth case for bumps with $h = 0.30$ and $h = 0.40$, and $M_\infty \geq 0.7$, considering different domains.

in figure 6 for some selected frequencies. The DNS simulations used a wave packet disturbance. The PSE code was obtained from Juniper, Hanifi & Theofilis (2014). The amplitude of each mode obtained by the PSE code was matched to the DNS at $x = x_R = 320.82$. Two measures of amplitude were used, namely, energy (based on $E = \int_0^{y_f} \frac{1}{2}(|\widehat{u'}|^2 + |\widehat{v'}|^2)\,\mathrm{d}y$) and the maximum amplitude of the fluctuating streamwise

998 A11-12
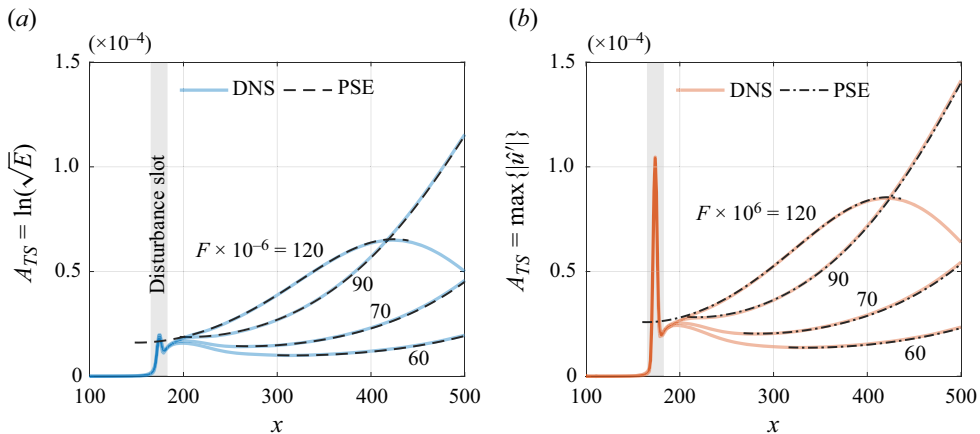
Figure 6. Amplitude evolution for TS waves of selected frequencies along the smooth plate obtained by the present DNS code at $M_\infty = 0.1$ and by the incompressible linear PSE. (*a*) Amplitude is based on the integrated fluctuation energy and (*b*) based on the maximum streamwise-velocity fluctuation. Here, $Re_{\delta*} = 950$ at the bump location.

velocity along the wall-normal direction ($|\widehat{u'}|_{max}$). The good agreement confirms that the packet evolution is linear and accurate and that our $M_\infty = 0.1$ simulations are effectively incompressible.

3.3. *Comparison with literature*

Results are compared with those of Wörner *et al.* (2003) that investigated the effect of rectangular two-dimensional bumps on the evolution of the TS wave of $F = 49.34 \times 10^{-6}$. The reference presented incompressible results, hence we used $M_\infty = 0.1$. The Reynolds number based on the conditions of the smooth plate at the roughness centre is $Re_{\delta*} = 1088$. The bumps had a length of $L = 20$ and the heights were $h = 0.235$ and $h = 0.470$. The TS wave of $F = 49.34 \times 10^{-6}$ ($\omega = 5.37 \times 10^{-2}$) was included by using the monochromatic excitation disturbance (2.8*a,b*) with the amplitude of $A_D = 1 \times 10^{-5}$. The excitation slot was centred at $x_D = 254.8$ ($Re_{\delta*} = 906$) and extended along the length $L_D = 33.6$.

Figure 7(*a*) shows the evolution of the TS wave amplitude we obtained for these bumps. Wörner *et al.* (2003) report that the bumps of $h = 0.235$ and $h = 0.470$ were responsible for an amplitude increase of 1.4 and 3.2 compared with the smooth plate. They report that their simulations overestimated the amplitude obtained in their corresponding experiments by 7 %. Figure 7(*b*) shows the results we found for the far downstream amplification factor relative to smooth and the results from Wörner *et al.* (2003). Perfect agreement with their experimental results is obtained.

4. Base flow and TS wave evolution

4.1. *Base flow*

In this section, we investigate how the incompressible boundary layer is deformed by the inclusion of a bump. The bumps are located at $Re_{\delta*} = 950$ ($x_R = 320.8$) for a physical domain extending up to $Re_{\delta*} = 1210$ ($x = 520.0$). This value of $Re_{\delta*}$ is the same as that of de Paula, Würz & Medeiros (2008); de Paula *et al.* (2017). The base flow shows important
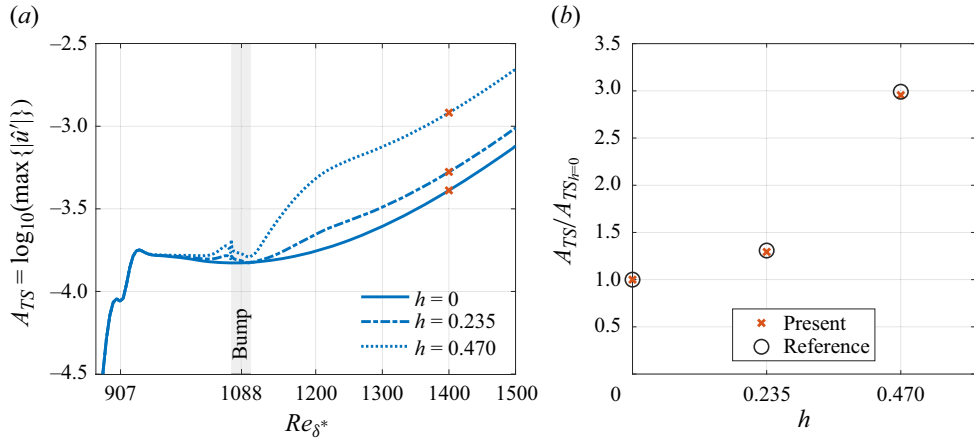
Figure 7. (*a*) Current DNS results of the TS wave ($F = 49.34 \times 10^{-6}$) amplitude evolution for selected cases investigated by Wörner *et al.* (2003). (*b*) Far downstream ($Re_{\delta^*} = 1400$) amplification factor relative to the smooth case compared with that from Wörner *et al.* (2003). Bumps are centred at $Re_{\delta^*} = 1088$ and have a length of $L = 20$. $M_\infty = 0.1$.

features that can affect the evolution of TS waves. Figure 8 presents the streamlines in the bump region. A region of recirculating flow (red streamlines) is formed immediately behind the bump. For each case, the reattachment point ($\partial u/\partial y|_{wall} = 0$) is indicated by a red marker. Even for $h = 0.05$ a very small recirculating flow region is formed, however, as it reattaches on the bump lateral edge, for this case we considered $x_{reattach} = x_{R_{TE}} = x_R + L/2$. Figure 9 shows how the recirculation length, L_{recirc} scales with h. For heights above $h = 0.20$ a parabola fits the data very well.

Figure 10(*a,b*) shows the deviation caused by the bumps on both the streamwise and wall-normal velocity profiles, at selected *x*-stations downstream of the bump. Hereinafter, we refer to this as profile deviation. For each station, *y* is normalised by the local Blasius displacement thickness, δ_B^*. The maximum deviations for $h = 0.40$ are indicated for reference. For both velocity components, the deviation essentially decreases in magnitude with the maximum located progressively farther from the wall. At each *x*-station, the profile deviations are very similar for all bumps, except for the recirculating flow region. This exception is noted particularly for the *v*-profile deviation at the two initial stations for $h = 0.40$.

The maximum deviation of ($u - u_B$) is fairly large for the bumps. As a reference, in order to cause a deviation of -0.175 ($h = 0.40$) the shape factor (m) of the Falkner–Skan profile family would have to be $m = -0.06$. Moreover, the maximum deviation of the Falkner–Skan profiles occurs at approximately $y/\delta_B^* = 1.2$, while for the bump wake profiles in figure 10(*a*), they occur, in general, much closer to the wall. This is important because the closer to the wall the deviation is, the stronger its impact on the stability of the boundary layer.

The distributions of the displacement thickness (δ^*), momentum thickness (θ) and shape factor (H) are plotted in figure 11(*a,b*). The deviation from the Blasius profile increases with h. The value of δ^* presents a maximum deviation just upstream of the bump trailing edge. The θ deviation oscillates in the bump region. There is a global maximum just upstream of the bump leading edge, a global minimum right at the bump leading edge and a local maximum downstream of the bump. In spite of that, these plots indicate that the smooth case Blasius profile is asymptotically recovered downstream. Figure 12(*a,b*) shows the evolution of $H - H_B$ normalised by h as a function of the distance from the
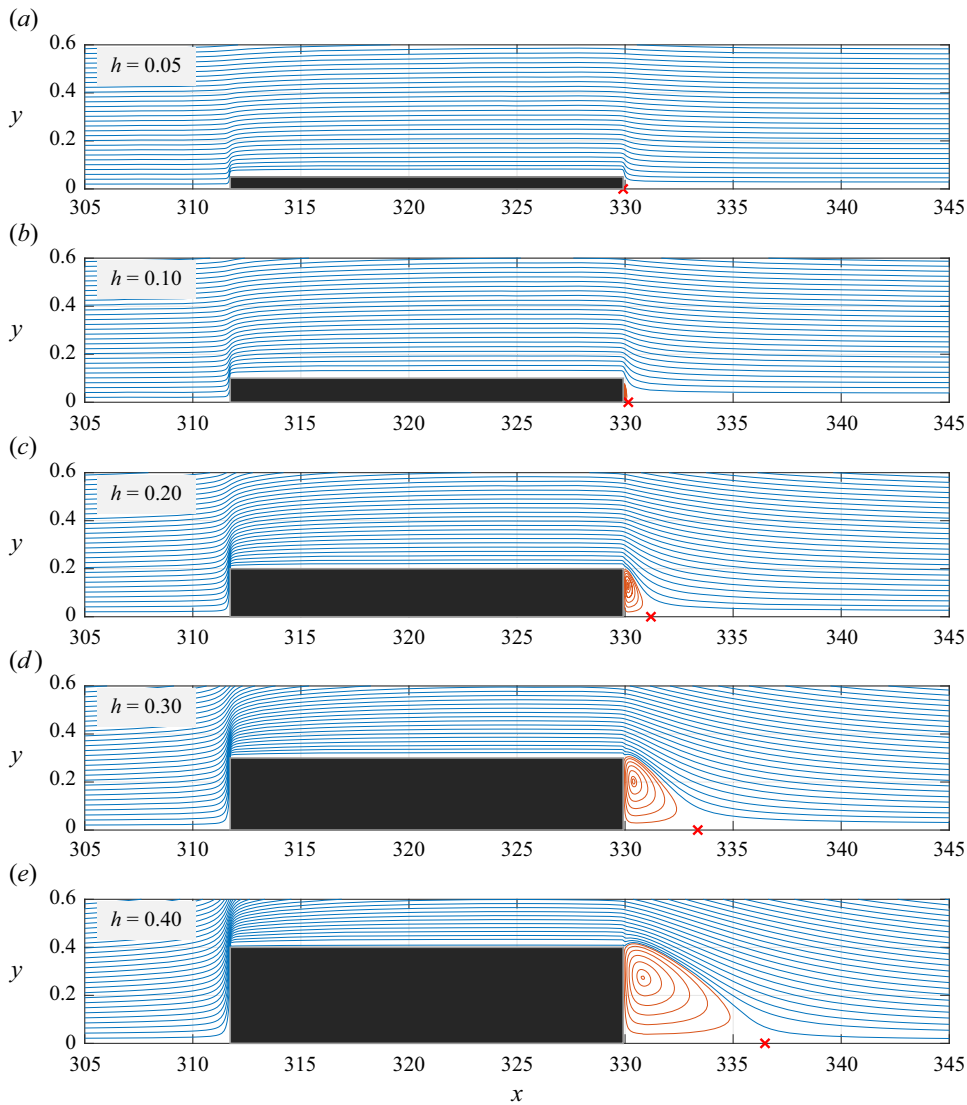
998 A11-14

Figure 8. Streamlines for cases with bumps of different heights. The red streamlines indicate the recirculating flow region that reattaches on the plate at $x_{reattach}$ marked with red symbols. In all cases, the bumps are located at $Re_{\delta*} = 950$ and have $L = 18.2$. Here, $M_\infty = 0.1$.

leading edge and from the reattachment point for each bump, respectively. Along the bump and the recovery region, the shape factor deviation, $H - H_B$, scales linearly only up to $h = 0.10$ as shown by the collapse of the curves in red and blue. Above it, the shape factor deviation increases nonlinearly with the bump height. A higher bump naturally produces a higher deviation. However, higher bumps also are exposed to a higher flow speed, which should further distort the profiles. We believe this is a possible explanation for the nonlinear scaling observed. Along the recovery region, the deviation evolves similarly in particular if each evolution is shifted by the respective reattachment point. nevertheless, the recovery region extension is not substantially affected by the bump height. For all heights $(H - H_B)/h < 0.01$ occurs nearly at the same location, $x \approx 420.0$ (≈ 90.0 relative to the bump).
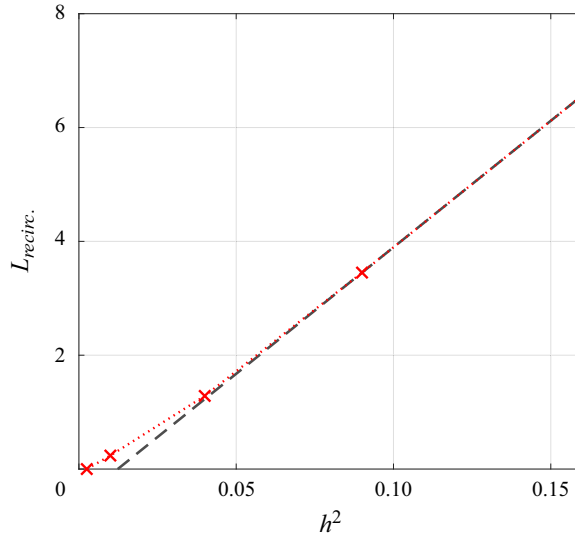
Figure 9. Length of the recirculating flow region vs bump height squared. The dashed line denotes a quadratic function fitting the length given by $h = 0.30$ and $h = 0.40$. Bumps centred at $Re_{\delta*} = 950$ with length $L = 18.2$. Here, $M_\infty = 0.1$.

4.2. *The TS wave*

Next, we evaluate the impact of the bump on the evolution of a TS wave. The simulations used wave packet disturbances, but in this section the analysis was performed for a single frequency. This is adequate since our analysis is restricted to the linear regime, as shown in § 3.2. The following sections analyse the full packet. The disturbance was excited along a slot centred at $Re_{\delta*} = 700$ ($x_D = 173.7$). In the present section, the TS wave had the frequency $F = 90 \times 10^{-6}$, which roughly represents the dominant TS wave at the end of the physical domain considered. The bump length is $L = 18.2$. Figure 13 shows the evolution of the TS wave maximum amplitude. As the TS wave travels, it destabilises along the region upstream of the bump, then it stabilises along the bump element and, finally, destabilises in the wake. These three stages of the TS wave evolution under the influence of the bump were also observed by Nayfeh *et al.* (1988) and Wörner *et al.* (2003). The fact that the TS wave reduces in amplitude along the bump should not be taken as surprising. The TS instability depends on a particular arrangement of velocity profiles close to the wall. This balance is affected by the profile distortions caused by the bump. It would be rather surprising if, instead, a large increase in the TS wave was seen on the bump. Figure 13 shows that, despite the relatively large fluctuations along the bump element, up to the bump trailing edge, the net impact is negligible. This is shown by the fact that, at the trailing edge of the bump, the curves for all the bump heights converged to the smooth plate curve. The dominant and enduring effect occurs in the wake region where the TS wave is massively amplified as the bump height increases. Far downstream of the bump, the TS wave amplitude evolves almost parallel to the smooth case, which indicates the growth rate associated with the Blasius profile is recovered. The TS wave recovery region (as coined by Klebanoff & Tidstrom 1972) ends around $x \approx 420.0$ (figure 12), at the same location where the distortion caused by the bump on the Blasius profile becomes negligible.

The evolution of the growth rate deviation from Blasius ($\sigma - \sigma_B$, with $\sigma = (dA_{TS}/dx)/A_{TS}$), normalised by the bump height is shown in figure 14. This plot shows that $\sigma - \sigma_B$ scales linearly with the bump height up to $h = 0.10$. Since the deviation is
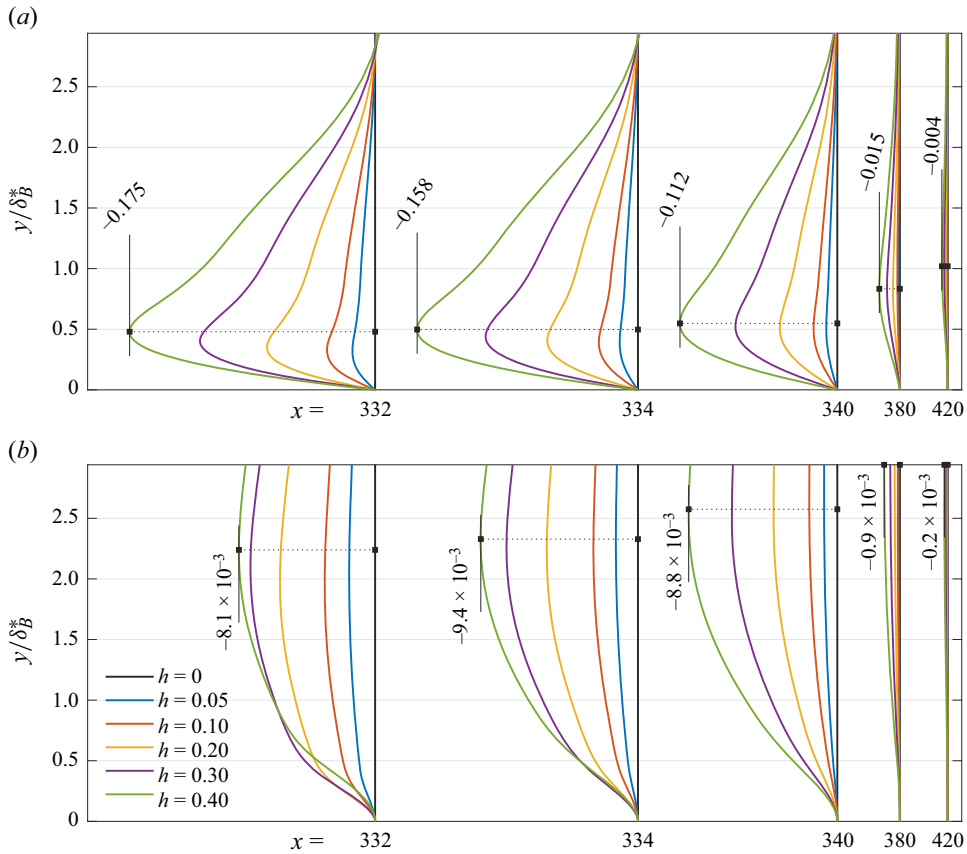
Figure 10. Velocity deviation profiles caused by bumps with different heights at selected stations in the bump wake. (*a*) Streamwise component ($u - u_B$) and (*b*) wall-normal component ($v - v_B$). Bumps are located at $Re_{\delta*} = 950$ and have $L = 18.2$. Here, $M_\infty = 0.1$.
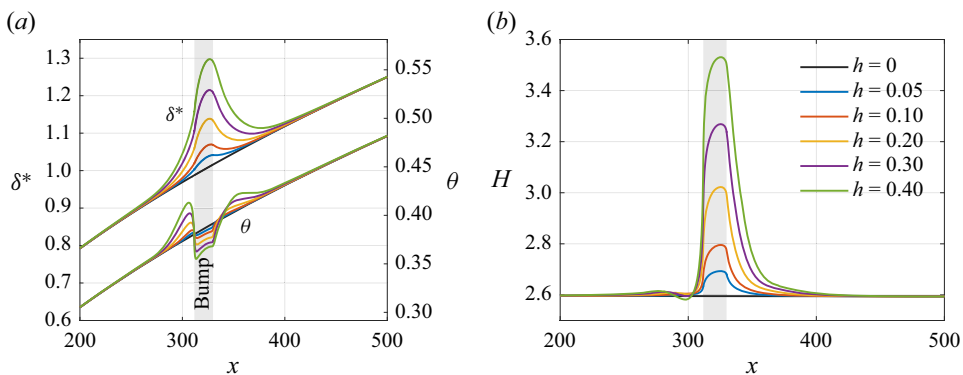

Figure 11. Bump effect on the boundary layer (*a*) displacement and momentum thicknesses, δ^* and θ, respectively, and (*b*) shape factor (H). Bumps at $Re_{\delta*} = 950$ with $L = 18.2$. Here, $M_\infty = 0.1$.
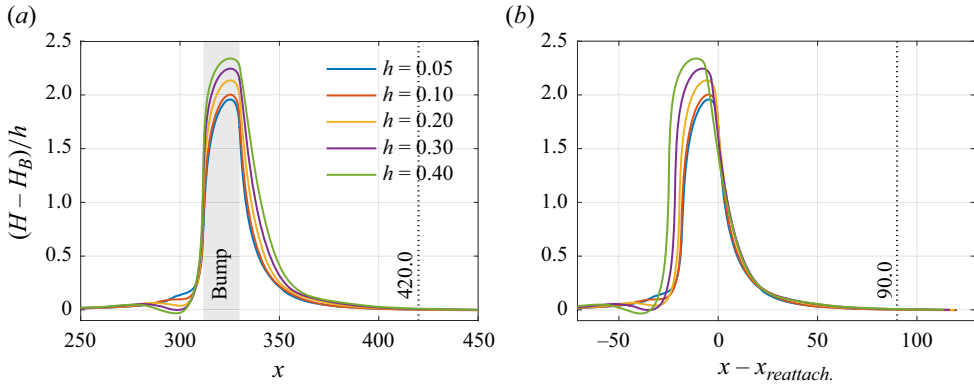
Figure 12. Evolution of the shape factor deviation normalised by h as a function of distance from (*a*) the plate leading edge and (*b*) the reattachment location ($x - x_{reattach.}$). Bumps at $Re_{\delta*} = 950$ with $L = 18.2$. Here, $M_\infty = 0.1$.
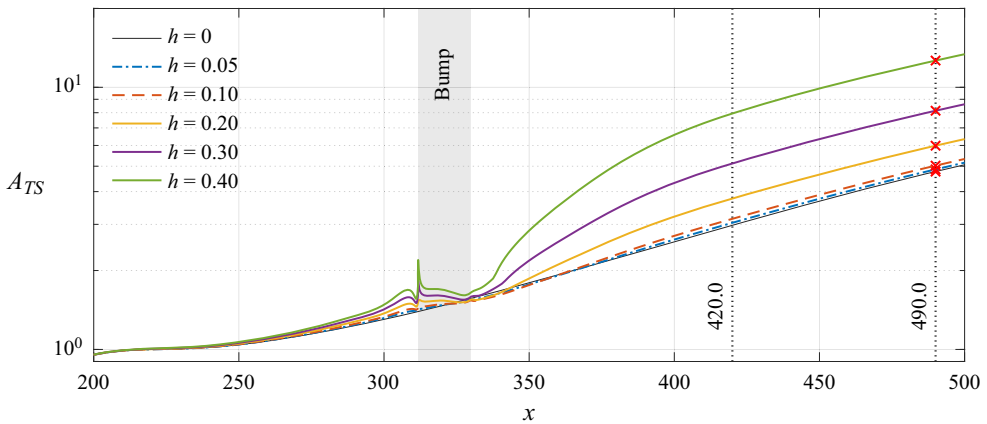
Figure 13. Amplitude evolution of the TS wave of $F = 90 \times 10^{-6}$ for different bump heights (normalisation considers the TS amplitude at $x = 200.0$). The bumps are located at $Re_{\delta*} = 950$ and have $L = 18.2$. Here, $M_\infty = 0.1$.

normalised by h the linear scaling up to $h = 0.1$ is shown by the collapse of red and blue curves. Above $h = 0.10$, the growth rate deviation varies nonlinearly with h, most of the nonlinear activity taking place very close to the bump. Consistent with the analysis above (figures 10–12), in this $h-$ normalised scale, the location where the smooth plate behaviour is recovered is around $x \approx 420.0$, independent of bump height.

The fact that the growth rate deviation scales linearly with bump height is noteworthy. This deviation is associated with the profile deviation, which up to $h = 0.10$, scales linearly with h. So the results in figure 14 are consistent. In turn, where the growth rate deviation scales linearly with h, the TS wave amplification factor associated with the bump should scale exponentially. Figure 15 presents the amplification factor vs h at $x = 490.0$ (indicated by the red markers in figure 13) but any x-station downstream of $x = 420.0$ (end of the recovery region) provides the same results. Consistent with the arguments above, up to $h = 0.10$ the amplification factor associated with the bump should scale as $\exp(c_1 \times h)$. This expression was fit to the two smaller bump results, including the smooth case, and provided
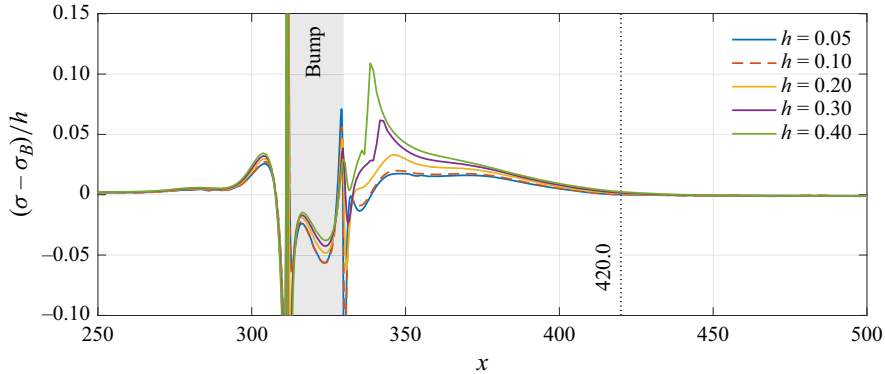
998 A11-18

Figure 14. Evolution of the growth rate deviation normalised by h for the TS wave of $F = 90 \times 10^{-6}$. The bumps are located at $Re_{\delta*} = 950$ and have $L = 18.2$. Here, $M_\infty = 0.1$.
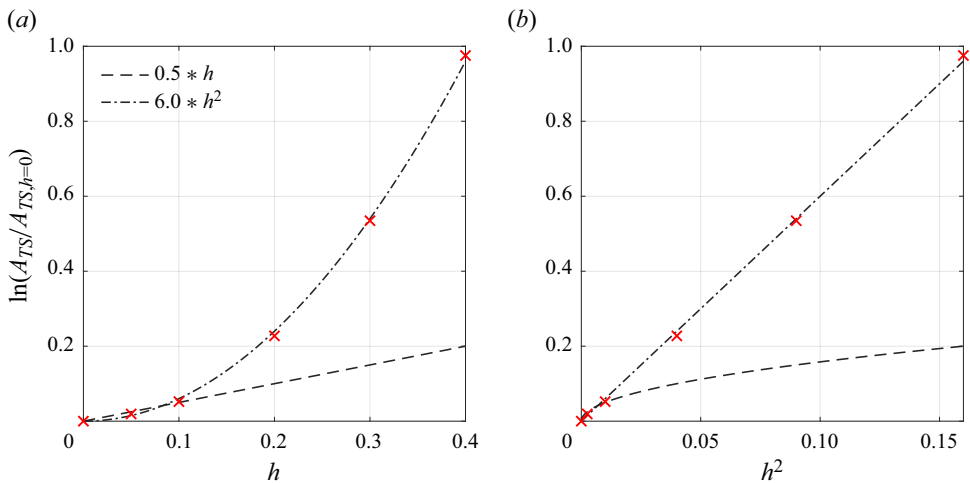

Figure 15. Amplification factor vs (*a*) h and (*b*) h^2 at the x-station $x = 490.0$ indicated in figure 13. The lines are best-fit curves. The bumps are located at $Re_{\delta*} = 950$ and have $L = 18.2$. Here, $M_\infty = 0.1$.

$c_1 = 0.5$. According to figure 14, above $h = 0.10$ the amplification factor should scale super-exponentially. As shown in figure 15, a good fit was obtained for $\exp(6.0 \times h^2)$.

5. Effect of Reynolds number on the base flow

This section investigates the effect of the Reynolds number on the base flow deviation caused by a bump. In addition to the $Re_{\delta*} = 950$ case, we considered bumps placed at $Re_{\delta*} = 1500$ and $Re_{\delta*} = 2000$. The bump heights were fixed to $h = 0.40$ relative to the local displacement thickness of each Reynolds number. In all cases, the non-dimensional bump length was fixed to $L = 18.2$, which is the same as for $Re_{\delta*} = 950$. The Mach number was set to $M_\infty = 0.1$ (incompressible).

Figure 16 compares the streamlines for the bump placed at different Reynolds numbers. Consistent with the observations of Klebanoff & Tidstrom (1972), the length of the recirculating flow region increases with $Re_{\delta*}$. For a fixed bump height, the recirculation region length roughly scales linearly with Reynolds number, figure 17.

(a)

$Re_{\delta*} = 950$

(b)

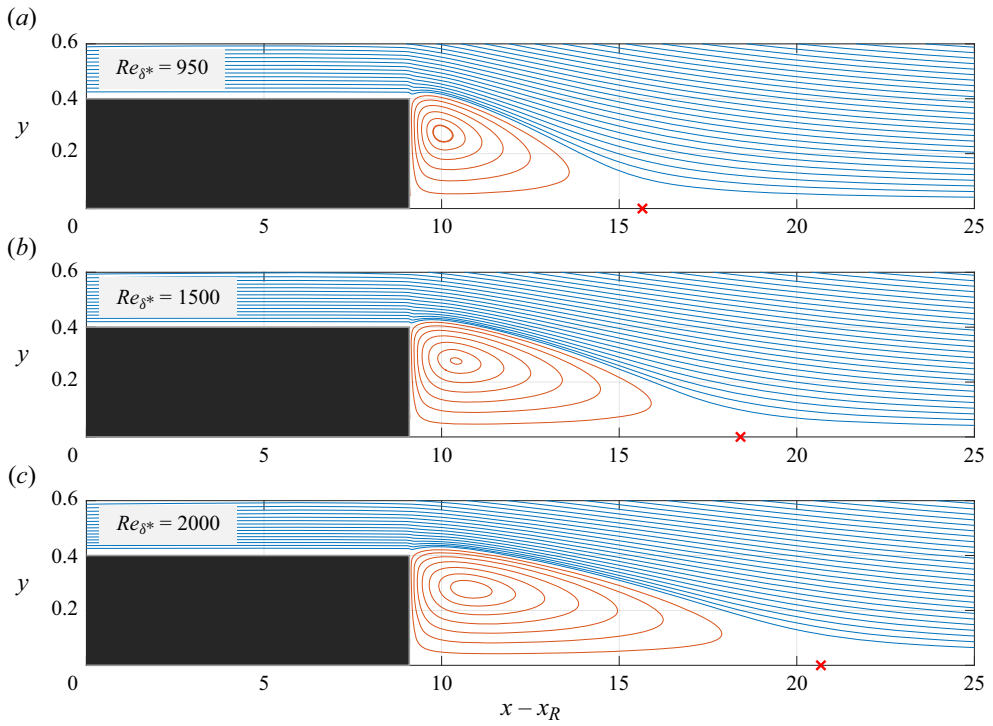$Re_{\delta*} = 1500$

(c)

$Re_{\delta*} = 2000$

$x - x_R$

Figure 16. Streamlines for cases with bump $h = 0.40$ placed at different $Re_{\delta*}$. The red streamlines indicate the recirculating flow region that reattaches to the plate at $x_{reattach}$ marked with red symbols. Here, $M_\infty = 0.1$ and $L = 18.2$.
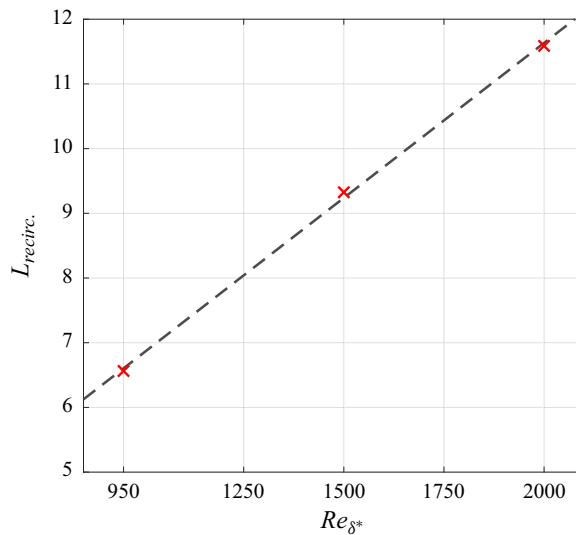
Figure 17. Length of the recirculating flow region as a function of $Re_{\delta*}$, for the bump with $h = 0.40$ located at $Re_{\delta*} = 950$. Here, $M_\infty = 0.1$ and $L = 18.2$.
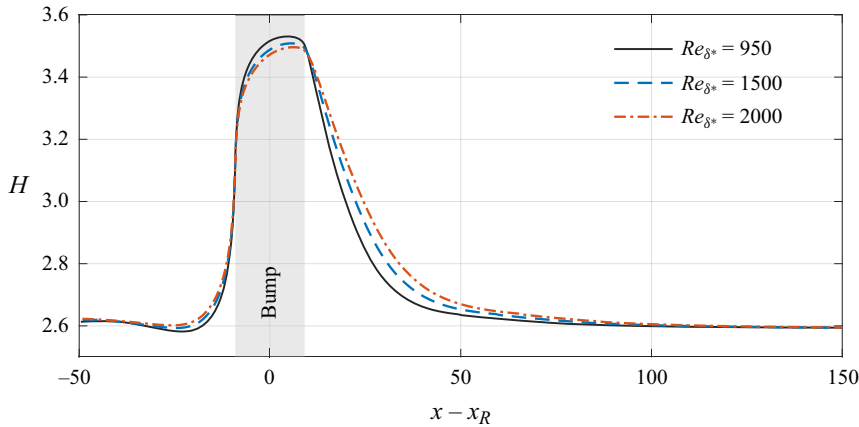
Figure 18. Effect of the bump Re_{δ^*} on the boundary layer shape factor (H), for $h = 0.40$. Here, $M_\infty = 0.1$ and $L = 18.2$.
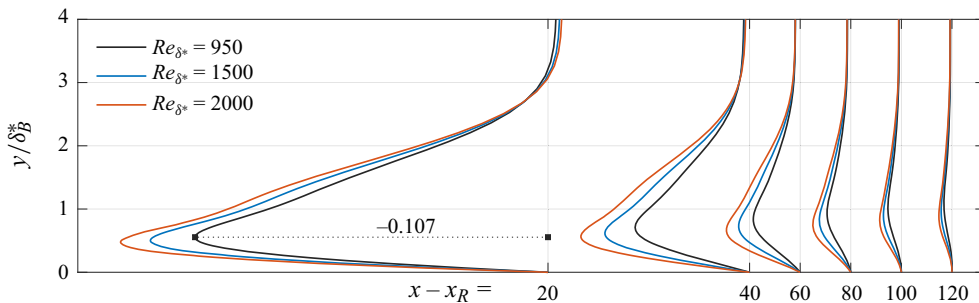

Figure 19. Streamwise-velocity deviation profiles, $u - u_B$, caused by a bump of $h = 0.40$ at different Re_{δ^*}. Here, $M_\infty = 0.1$ and $L = 18.2$.

Figure 18 shows the effect of the Reynolds number on the shape factor (H) evolution. The curves indicate that the Reynolds number influences mainly the bump wake. It does not only increase the extent of the wake but also the magnitude of the shape factor deviation. The deviation velocity profiles are shown in figure 19. The Reynolds number affects the deviation magnitude, but not its distribution. It is known that the Reynolds number does not affect the shape of the laminar wake (Schlichting & Gersten 2000). Our observations of the bump wake are consistent with these results. As the bumps have the same height relative to the local Blasius profile δ_B^*, it is expected that the Reynolds number would not affect the shape of the laminar wake. The process by which the deviation profile vanishes is governed by diffusion. As the Reynolds number increases, the diffusion reduces relative to the convection in the boundary layer. Therefore, the wake requires a longer extension to return to the Blasius profile as the Reynolds number increases. This explains part of the destabilising influence of the Reynolds number on the effect of a bump on a TS wave evolution.

6. Effect of frequency and Reynolds number on the TS wave–bump interaction

Here, we extend the analysis to account for the effect of Reynolds number on the TS wave–bump interaction. As will be seen, it is intertwined with an effect of TS
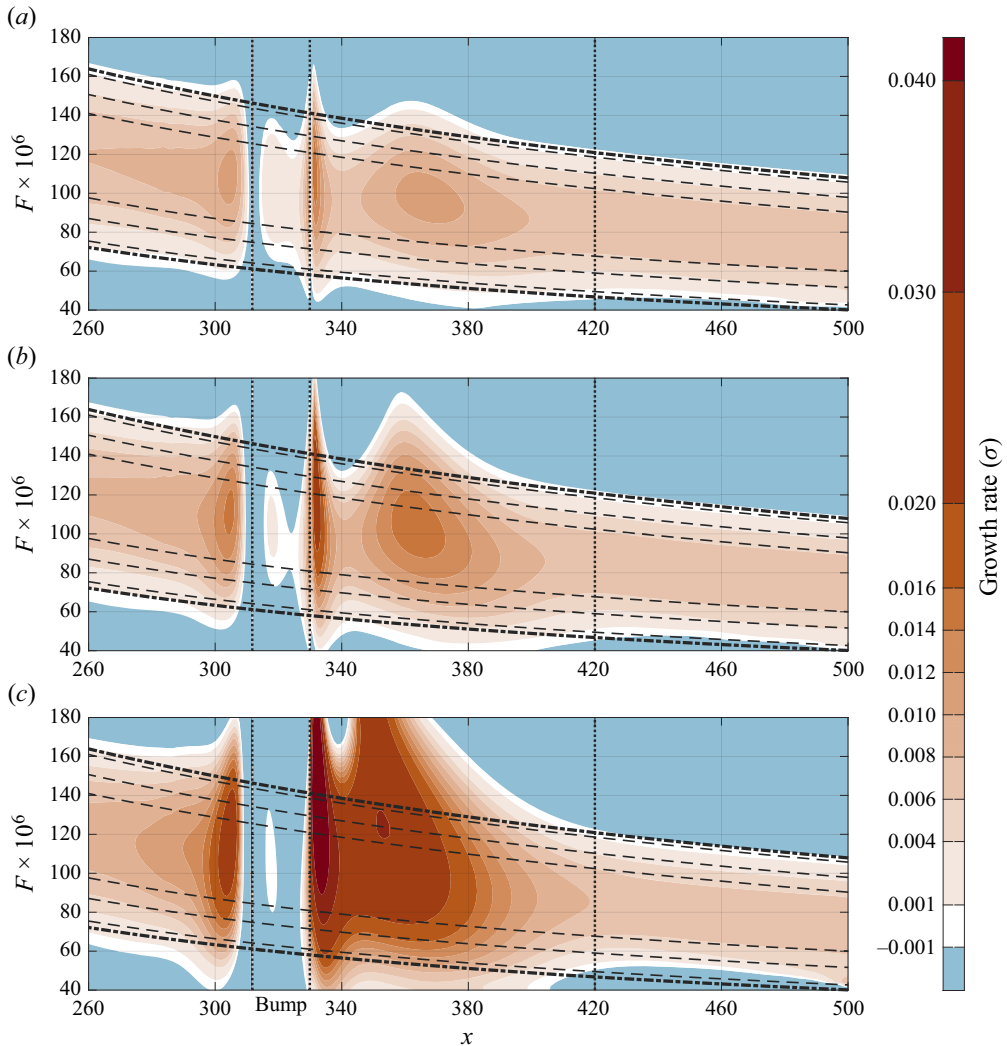
Figure 20. Contours of growth rate for bumps with $h =$ (*a*) 0.10, (*b*) 0.20 and (*c*) 0.40. Black-dashed lines denote iso-levels of $\sigma = [0.001; 0.004; 0.006]$ for a smooth plate case, the dash-dotted lines are the neutral curves. Here, $Re_{\delta*} = 950$, $M_\infty = 0.1$ and $L = 18.2$.

wave frequency. Figure 20 shows contours of growth rate as a function TS wave frequency along the streamwise direction, for bumps located at $Re_{\delta*} = 950$ with heights $h = 0.10$, 0.20 and 0.40. These results were obtained with simulations of the evolution of wave packets. As observed in figure 20, the frequency range of the packets ensured that all relevant modes were excited. These plots extend in frequency the analysis from § 4.2. We observe two distinct regions characterised by an increase in the growth rate that was not clearly apparent when focusing solely on the frequency of $F = 90 \times 10^{-6}$ (see figure 14). The first region is that corresponding to the recirculation flow (see figure 16) where the growth rate is notably high, albeit extending only for a short distance from the bump. The second region is in the far wake where the increase in the growth rate is comparatively lower, but persists over a much longer distance. As the latter exerts a more sustained influence, the effect along the far wake tends to be dominant. We are not confident on the

stabilising effect observed downstream of $x = 420.0$ around the lower branch, more clearly noticed for $h = 0.40$. The evolution of TS waves with such low frequencies becomes progressively more compromised because they may not have been fully established before reaching the bump. In any case, these frequencies are so low that do not contribute to the N-factor curves discussed below and hence do not affect the conclusions of the paper. The contour plots in figure 14 are consistent with those presented by Xu *et al.* (2017), Thomas, Mughal & Ashworth (2017) and Thomas *et al.* (2018). For instance, their results show an increase in the growth rate right at an indentation while ours show a reduction in the growth rate right at the bump.

The contours in figure 20 also show that along the bump wake the impact on the growth rate is much stronger for the TS waves around the upper branch. This is what leads to the upward shift in the frequency of the dominant TS wave, observed in early studies (Klebanoff & Tidstrom 1972; Nayfeh *et al.* 1988; Masad & Iyer 1994). Recall that the base flow deviation along the wake profiles (see figure 10a) also resembles that caused by the presence of an adverse pressure gradient. The adverse pressure gradient extends the unstable region of the instability diagram (Schlichting & Gersten 2000) mostly by moving the upper branch upwards. We refer to this phenomenon as the upper branch effect. Clearly, besides the effect of frequency, this also incorporates an effect of the Reynolds number at the bump location.

To better substantiate the effect of the Reynolds number we run simulations with a bump of $h = 0.40$ placed on two other locations ($Re_{\delta*} = 1500$ and 2000). The results of the n- and the N-factor evolution are shown in figure 21(a). Here, the n-factor corresponds to a TS wave amplification for a single frequency, $n(x) = \ln(A_{TS}(x)/A_{TS,0})$, where $A_{TS,0}$ corresponds to the TS wave amplitude at the lower branch. The N-factor corresponds to the envelope of the n-factor evolution curves for all frequencies at all x-stations. Figure 21(b) shows the change on the n- and the N-factors for the bump cases relative to that from the smooth one (black lines in figure 21a). Both pictures display clearly that the higher the Reynolds number the larger the impact of a given bump. This result incorporates both the effect of the Reynolds number on the base flow and the upper branch effect.

Figure 21 also illustrates another interesting aspect associated with the upper branch effect that affects the ΔN curves. The frequency of the TS wave at the transition location reduces as the transition moves downstream independently of the presence of the bump. However, the lower frequencies are less affected by the bump, as also seen by Klebanoff & Tidstrom (1972) and Wang & Gaster (2005). Consequently, while the Δn curves tend asymptotically to a constant value, the ΔN curves decrease even downstream of the recovery region. Because of that, the effective ΔN factor depends also on the magnitude of the TS wave content in the boundary layer. For example, from figure 21, if the environment is such that $N_{cr} = 5$, for a bump at $Re_{\delta*} = 1500$ (red curve), the transition would occur around $Re_{\delta*} \approx 1600$, with a $\Delta N = 1.8$. For the same bump in a reduced noise level environment such that $N_{cr} = 7.5$, the transition would occur at $Re_{\delta*} = 2400$ with $\Delta N \approx 1.1$. An almost 40% reduction in the ΔN.

As an example, the overall effect of the Reynolds number can be quantified as follows. Suppose that transition occurs at $Re_{\delta*} = 2150$ for the bump at $Re_{\delta*} = 2000$ (yellow curve in figure 21). In this case, $\Delta N = 2.3$ and $N_{cr} = 7.6$. On the other hand, for the bump at $Re_{\delta*} = 1500$, the transition would occur at $Re_{\delta*} = 2400$ with $\Delta N = 1.1$. For the bump located at $Re_{\delta*} = 950$, ΔN would be approximately 0.5 or less, with an almost negligible impact on transition. A twofold variation in Reynolds number could lead to more than fourfold variation in ΔN. Recall that these variations in ΔN incorporate both the effect of the Reynolds number on the base flow and the upper branch effect. We quantified these
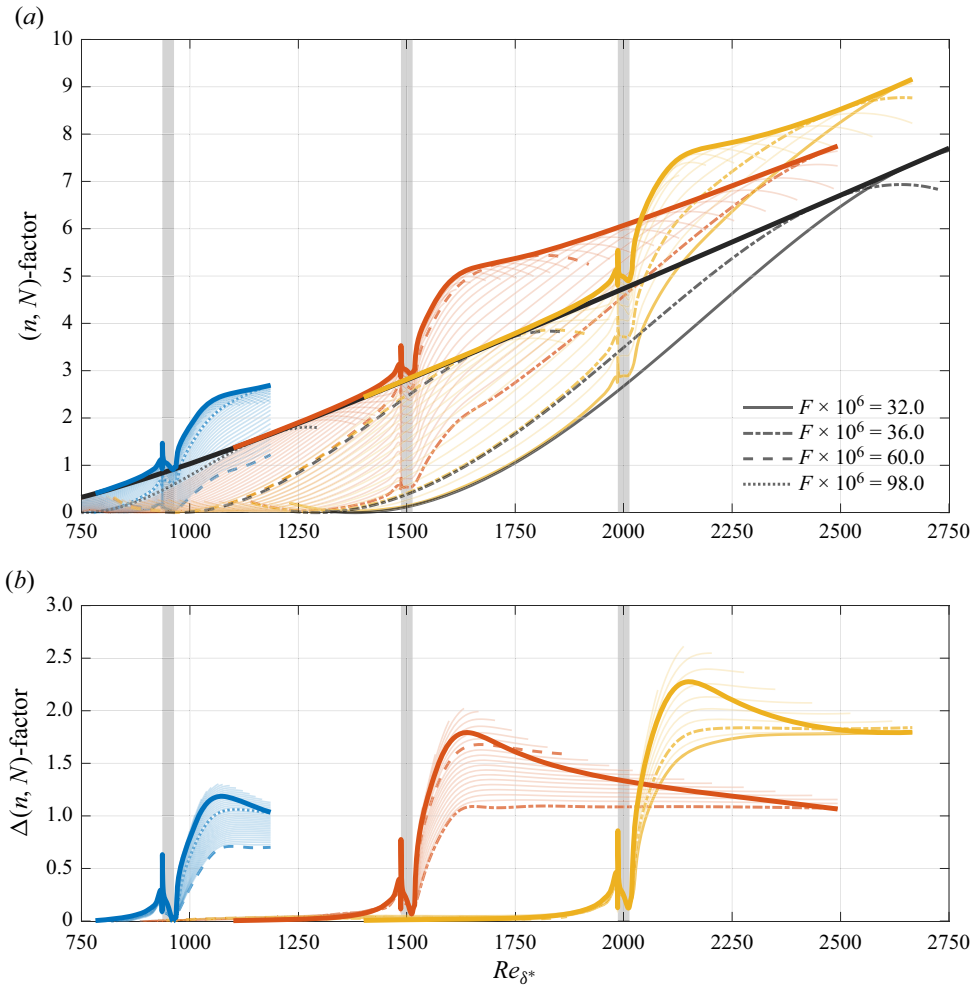
Figure 21. (*a*) The *n*-factor (thin lines) and *N*-factor (thick lines) evolution for a bump of $h = 0.40$ placed at $Re_{\delta*} = 950$, $Re_{\delta*} = 1500$ and $Re_{\delta*} = 2000$; (*b*) *n*- and *N*-factor change relative to those from the smooth plate. For selected TS frequencies the *n*-factor curves are highlighted and indicated by different line styles. For these modes, results from PSE calculations (black lines) are also shown for reference. Here, $M_\infty = 0.1$ and $L = 18.2$ in all cases.

effects as ratios between two values of ΔN because these ratios should remain similar for bumps of other heights at these locations. These ratios are very significant and neglecting these effects should lead to inaccuracy in transition prediction.

Figure 21 also shows that the bump causes a frequency shift. It does not represent the difference in the TS frequency at the transition location for a bump case relative that of the smooth one. The frequency shift is on the dominant TS wave at each *x*-station (Himeno *et al.* 2023). It is associated with the difference between the dotted blue line, the dashed red line and the dashed-dotted yellow line and their respective envelopes. This shift depends on the bump height and Reynolds number, but in the current parameter space, it represents an error in ΔN below 0.1, which is not relevant for predictions.

There are some studies in the literature that present results for different bump-location Reynolds numbers. However, only two studies (Klebanoff & Tidstrom 1972; Masad & Iyer 1994) were found that gave enough detail for the analysis below. Klebanoff & Tidstrom
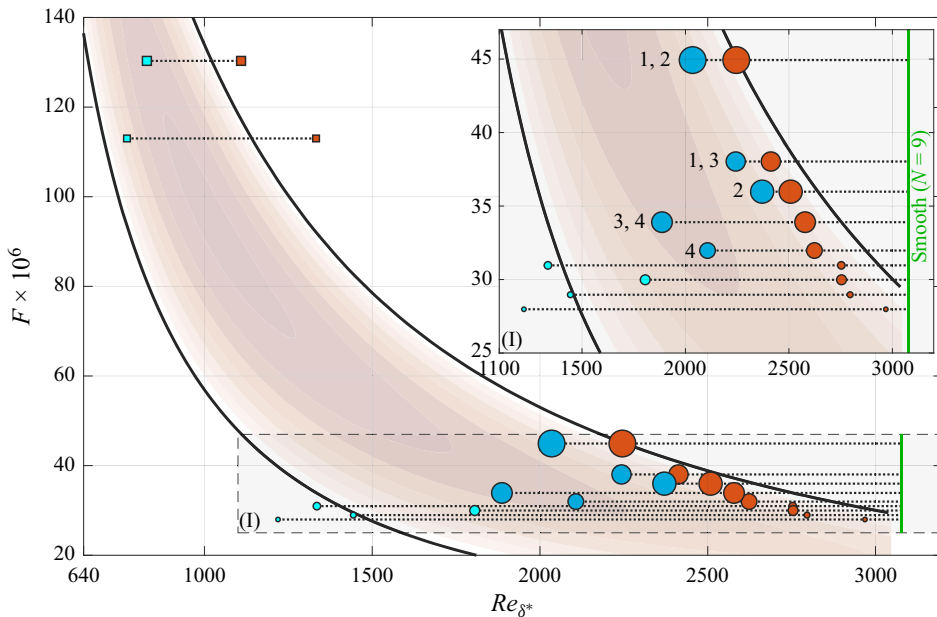
Figure 22. Data extracted from Klebanoff & Tidstrom (1972) (squares) and Masad & Iyer (1994) (circles) plotted over the instability diagram. The Reynolds numbers at the bump are indicated by light- ($h < 1.0$) and dark-blue ($h \geq 1.0$) symbols. The Reynolds number at the transition locations are shown by the red symbols. For each case, the frequency corresponds to that which is critical at the transition location.

(1972) is a wind tunnel experiment that measured the impact of circular-section bumps (wires) on the transition location under natural conditions. Masad & Iyer (1994) give a theoretical study of the impact of smooth-shaped bumps (humps) using the IBL method and linear stability analysis to obtain the amplification of the TS waves. In Masad & Iyer (1994), the transition location is based on the e^N method with $N_{cr} = 9$. The use of $N_{cr} = 9$ could be questioned, but the conclusions of the analysis do not depend on the value of N_{cr}. These data are interesting also because they extend the parameter space towards bumps substantially larger than ours. Klebanoff & Tidstrom (1972) used bumps with $h = 0.72$ and $h = 0.77$ and for the selected cases from Masad & Iyer (1994), the heights are between $h = 0.58$ and $h = 1.17$. These studies also extend the analysis to include other methods, namely, experiment and theory, while ours is numerical.

The results are plotted in figure 22, on top of the smooth plate instability diagram. The squares represent the Klebanoff & Tidstrom (1972) results and the circles those of Masad & Iyer (1994). The vertical green line indicates the transition Reynolds number for the smooth case from Masad & Iyer (1994). The red markers indicate the Reynolds number for the transition location ($N = 9$) with the bump. The blue markers indicate the Reynolds number at the bump location. The distance between the red marker and the green line gives the movement of the transition location caused by the bump. In the plot, for all markers the frequency was the dominant one at the transition location for the case with the bump. The bump shifts the dominant frequency upwards. The larger the transition point movement, the higher the frequency shift. There is a bump, located shortly above $Re_{\delta*} = 2000$, that causes the largest transition location movement and higher-frequency shift. For bumps upstream of this, the impact of the bump is given by the distance between the green line and the red markers, the displacement of the transition point. For bumps downstream of this location, the transition point movement is necessarily smaller than

the maximum, because the bump will not move the transition to a point upstream of the bump. The transition point is then so close to the bump that $N_{cr} = 9$ is reached upstream of the point of its maximum ΔN. In other words, the bump does contribute to transition with its full potential. For bumps at these positions, the magnitude of the bump effect is not measured by the distance between the smooth plate transition point (green line) and the bump case transition point (red markers). It is given by the distance between the bump position (blue marker) and the transition point for the bump case (red markers). Downstream of the critical position, the higher the bump impact the closer to the bump the transition occurs. There is clearly a bump position that moves the transition point the most, which is that for which the critical N is reached right where ΔN is maximum. For reference, we called it the critical position. This position would depend on the background noise and probably on the bump shape.

In figure 22, for each of the two references (Klebanoff & Tidstrom 1972; Masad & Iyer 1994), the size of the markers (square or circle) represents the relative magnitude of the bump height. The data were not meant to investigate exclusively the effect of either bump height or Reynolds number and for every bump-location Reynolds number, a different height relative to the local displacement thickness was used. Yet, useful information on the different effects can be obtained. By the way in which these tests were performed, in general, the larger bumps were placed at a higher Reynolds number, two effects that tend to produce a larger impact on transition, either by causing a larger transition movement (for bump upstream of the critical position) or by moving transition closer to the bump (for bumps downstream of the critical position). However, there are a few roughness pairs (indicated by the numbers 1, 2 and 3) for which a smaller bump was tested downstream of a larger one and had a higher impact. The bump impact is assessed by either comparing the length of the transition movement or by comparing the transition point proximity with the bump. There is also a case (indicated by 4) in which a smaller bump had almost the same impact as a larger one. In general the bump height has a higher impact, but for these 4 cases, the effect of Reynolds number is manifested. This phenomenon is apparent downstream of the maximum growth rates of the TS wave on a smooth plate, consistent with the arguments raised above about the effect of proximity to the upper branch. In fact, in the figure, it is noticeable that, under the influence of the bump, the transition occurs shortly upstream of the upper branch. This is also possibly an underlying manifestation of the upper branch effect.

In summary, the upper branch effect dictates that the bump impact increases the closer the bump is to transition. Under these circumstances, the TS wave leading to transition interacts with the bump closer to its maximum ΔN location. On the other hand, if the bump is located far upstream of transition, the TS wave that leads to transition interacts with the bump far from the point where it crosses the upper branch and the bump has a smaller impact on the TS wave. It is important to add that the results analysed in this section include both the effect of the Reynolds number on the base flow as well as the Reynolds number effect associated with the proximity to the upper branch. Both of them dictate that the bump effect is larger as the bump moves downstream, closer to the transition location. The upper branch effect also dictates that for a fixed bump location, if transition moves upstream (caused for example by an increase in free stream turbulence) the bump effect increases.

7. The combined effects of the bump height and local Reynolds number

The impact of a bump on the transition location has been evaluated in terms of several dimensionless parameters (Tani *et al.* 1940; Fage & Preston 1941; Dryden

1953; Carmichael 1959). One parameter widely used is a Reynolds number defined as $Re_{hh} = u_h^\star h^\star / \nu^\star$, where $u_h^\star$ denotes the streamwise velocity evaluated at the bump height for the smooth surface boundary layer. Considering the smooth case is a Blasius flow, for a bump with non-dimensional height $h = h^\star / \delta^{\star\star}$ placed at Re_{δ^*}, we can write $Re_{hh} = 0.571 \, Re_{\delta^*} \, h^2$ (Dryden 1953; Morkovin 1990). As the Re_{hh} parameter encompasses both the h and Re_{δ^*} effects, this parameter was not convenient to discuss the individual contributions of the bump height and of the local Reynolds number. However, the combined effects analysed in terms of the Re_{hh} give further valuable insight into understanding of the phenomenon.

First, recall some experimental results from Tani (1961) that investigated the impact of circular-section bumps (wires) on the transition location of a flat plate boundary layer. For each bump with fixed dimensional height ($h^\star$) and location ($x_R^\star$), Tani (1961) measured the transition location ($x_{tr}^\star$) as the free-stream velocity ($U_\infty^\star$) increased. As expected, for a fixed dimensional bump case, $x_{tr}^\star$ moves towards $x_R^\star$ as $U_\infty^\star$ increases. Tani (1961) also shows that, for each run, there exists a $U_\infty^\star$ such that the Reynolds number at the transition location, $Re_{x_{tr}} = U_\infty^\star x_{tr}^\star / \nu^\star$, reaches a minimum value, $(Re_{x_{tr}})_{min}$. For this particular condition, the transition does not occur at the roughness, but at some distance downstream. Tani (1961) also shows that the $(Re_{x_{tr}})_{min}$ condition was not related to a constant Re_{hh}, as previously stated by Dryden (1953), but varies along a range of Re_{hh}.

The condition which causes the lowest $Re_{x_{tr}}$ corresponds to the maximum bump impact relative to the smooth surface. Then, in the context of the e^N-method, such a $(Re_{x_{tr}})_{min}$ would correspond to a maximum ΔN condition, $(\Delta N)_{max}$. As shown in figure 21(*b*), the ΔN curves reach a maximum value not far downstream of the bump, consistent with the Tani (1961) results.

Figure 23 shows $(\Delta N)_{max}$ vs Re_{hh} for the cases presented in §§ 4–6. The value of $(\Delta N)_{max}$ scales almost linearly with Re_{hh} as indicated by the dashed line. This linear relation may indicate why Re_{hh} was taken as a good parameter to assess the effect of a bump on transition. The threshold value of $Re_{hh} = 25$, often assumed as the upper limit for the effectively smooth surface (Morkovin 1990), is indicated for reference. We note that there is not a Re_{hh} below which the $(\Delta N)_{max}$ is actually null. Nevertheless, for $Re_{hh} < 25$, the plot indicates a $(\Delta N)_{max} < 0.3$, which is likely to be within the uncertainty of measurements of the transition location in wind tunnels (Crouch & Kosorygin 2020), hence there is consistency in the results.

Figure 24 shows the recirculation length vs the Re_{hh} for the same cases shown in figure 23. The value of $L_{recirc.}$ also scales linearly with Re_{hh}, as indicated by the dashed line. In fact, since $Re_{hh} = 0.571 Re_{\delta^*} h^2$, such agreement was expected from figures 9 and 17, where we showed that $L_{recirc.}$ varies almost quadratically with h and linearly with Re_{δ^*}. Moreover, the results in figures 23 and 24 also suggest that $(\Delta N)_{max}$ is associated with the recirculating bubble in the bump wake.

8. The destabilising effect close to sonic speeds

In this section, we investigate the effect of compressibility for Mach numbers from 0.1 to 0.9, for bumps placed at $Re_{\delta^*} = 950$. In all cases, the TS waves were excited by the wave packet described by (2.9) with the parameters A_0, ω_0 and n_k shown in table 2. For all cases discussed in this section, the simulation set-up was the same as that for the $M_\infty = 0.1$ cases. Since the compressibility thickens the boundary layer, the effective non-dimensional bump heights ($h = h^\star / \delta^{\star\star}$) reduced with M_∞ compared with their nominal values ($h = 0.05, 0.10, 0.20, 0.30$ and 0.40) defined for $M_\infty = 0.1$. This reduction is generally small,
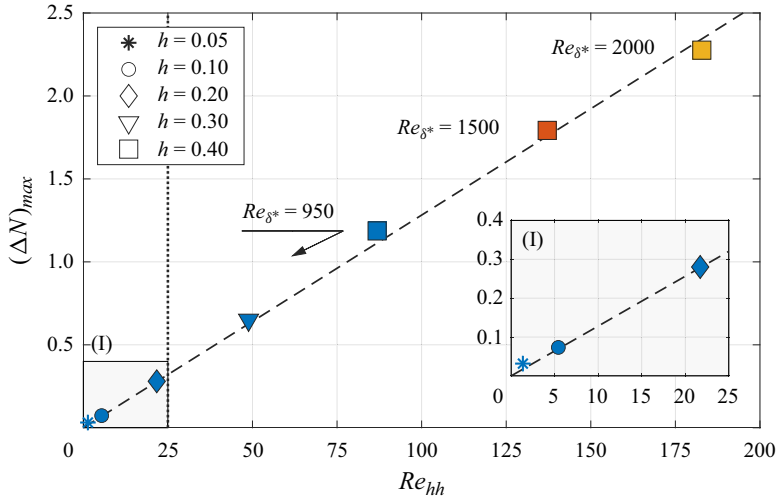
Figure 23. Value of $(\Delta N)_{max}$ vs the Re_{hh} for bumps of different h and placed at different $Re_{\delta*}$. The blue markers correspond to bumps placed $Re_{\delta*} = 950$, the red marker at $Re_{\delta*} = 1500$ and the yellow marker at $Re_{\delta*} = 2000$. For all cases, $M_\infty = 0.1$ and $L = 18.2$.
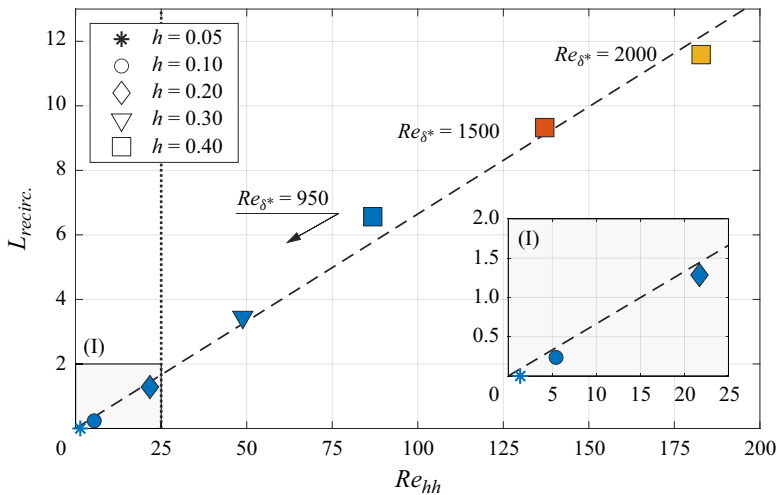

Figure 24. Value of $L_{recirc.}$ vs Re_{hh} for bumps of different h and placed at different $Re_{\delta*}$. The blue markers correspond to bumps placed $Re_{\delta*} = 950$ the red marker at $Re_{\delta*} = 1500$ and the yellow marker at $Re_{\delta*} = 2000$. For all cases, $M_\infty = 0.1$ and $L = 18.2$.

but as it becomes significant for the higher heights and higher Mach numbers, the effective height will be considered.

The disturbance slot was also the same as that for $M_\infty = 0.1$ cases. Hence, the effective $Re_{\delta*}$ at the disturbance position was different from the nominal one. However, this variation does not affect the conclusions because only the packet evolution far from excitation is relevant for the current analysis. In the far field, owing to the large amplification rates of the boundary layer, small variations in the excitation position do not significantly affect the packet evolution in the linear regime.
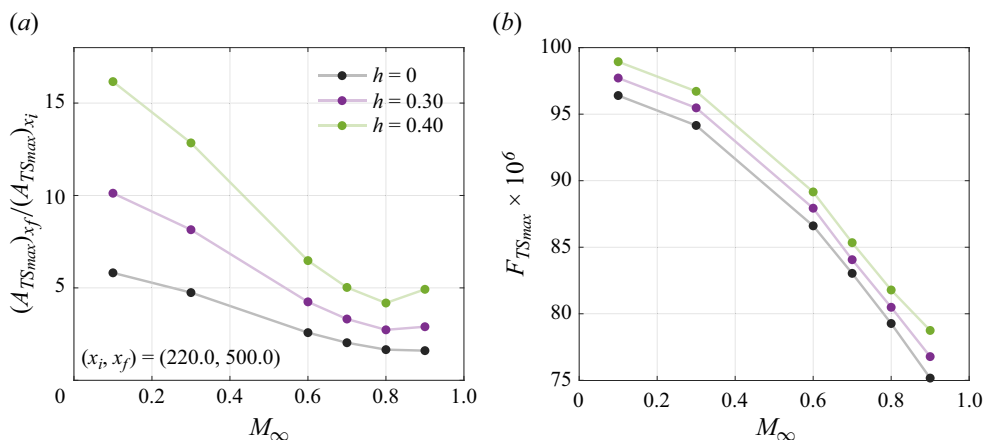
998 A11-28

Figure 25. Effect of Mach number on the amplitude and frequency of the dominant TS wave at $x = 500.0$. Bumps at $Re_{\delta*} = 950$ ($x_R = 320.8$) with length $L = 18.2$.

Figure 25(*a*) shows, for selected nominal bump heights, the effect of M_∞ on the amplitude of the dominant TS wave at $x = 500.0$. The corresponding frequencies are shown in figure 25(*b*). The results are qualitatively similar to those of Masad & Iyer (1994) for both the amplitude and frequency for $M_\infty \leq 0.8$, the Mach number range they investigated. The results show a stabilising effect of M_∞.

As anticipated, we have to consider that the boundary layer thickness increases with M_∞. The results presented in figure 25 are actually for lower values of bump height non-dimensionalised by the smooth plate boundary layer displacement thickness at the bump location, $\delta^*_{h=0}(x_R)$. The nominal height results suggest an apparent further stabilising effect of the Mach number. Figure 26 shows the variation of Δn with respect to the effective bump height, $h = h^\star/\delta^{*\star}_{h=0}(x_R)$. Note that h reduces as M_∞ increases. For each Mach number, Δn was calculated for the TS wave that is dominant at $x = 500.0$ for the smooth plate, i.e. for the frequencies shown by the black curve in figure 25(*b*). The Δn curves in figure 26 essentially collapse up to $M_\infty = 0.8$, but for $M_\infty = 0.9$, the curve diverges substantially from the others. The value of h reduces by approximately 5 %. As occurs in the incompressible regime (see figure 15), Δn varies almost quadratically with h, as indicated by the best-fit parabolas shown in grey in figure 26. We then used the quadratic fitting curves to estimate the Δn for the effective bump heights of $h = 0.05, 0.10, 0.20,$ 0.30 and 0.40 at every M_∞. The resulting curves are shown in figure 27.

Figure 27 presents results normalised by the smooth plate case. This removes the strong stabilising effect of M_∞ on the TS wave smooth plate evolution noticed in figure 25 and focuses on the influence of compressibility on the effect of a bump on a TS wave evolution. Note that, in figure 27, the curves correspond to the effective bump height since we resorted to the curves in figure 26. This more precise and clearer view indicates that the stabilising effect of compressibility prevails only up to $M_\infty = 0.7$. Above it, compressibility becomes progressively more destabilising, such that the magnitude of the bump impact at $M_\infty = 0.9$ is higher than that at $M_\infty = 0.1$.

In order to investigate the origin of the destabilising effect of compressibility we first investigated its impact on the base flow. Figure 28 presents the evolution of δ^*, θ and H, for selected bump heights and Mach numbers. The curves are normalised by the effective h. The maximum deviation of H occurs on top of the bump and is not substantially affected by Mach number. Upstream of the bump, the curves diverge, but as discussed previously,
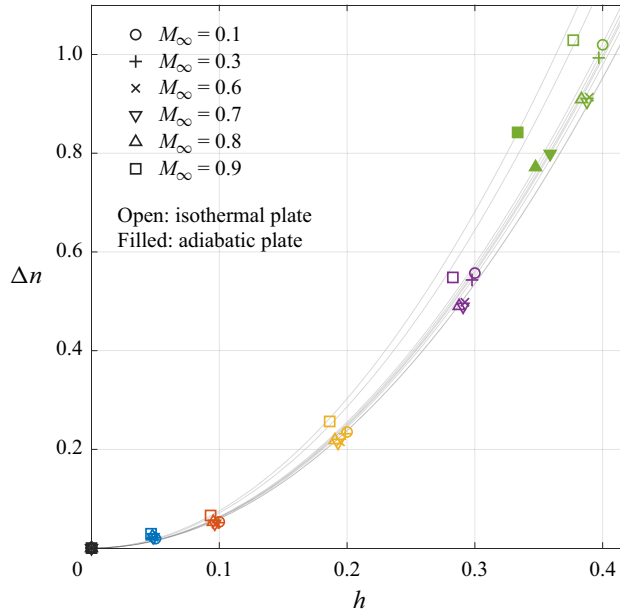
Figure 26. The Δn-factor vs the effective bump height ($h^\star/\delta^{*\,\star}_{h=0}(x_R)$) for each simulated Mach number and plate temperature condition. The colours of symbols indicate the nominal bump height. For each M_∞, the TS wave is that which is dominant at $x = 500.0$ considering the smooth case. Bumps at $Re_{\delta*} = 950$ ($x_R = 320.8$) with length $L = 18.2$.
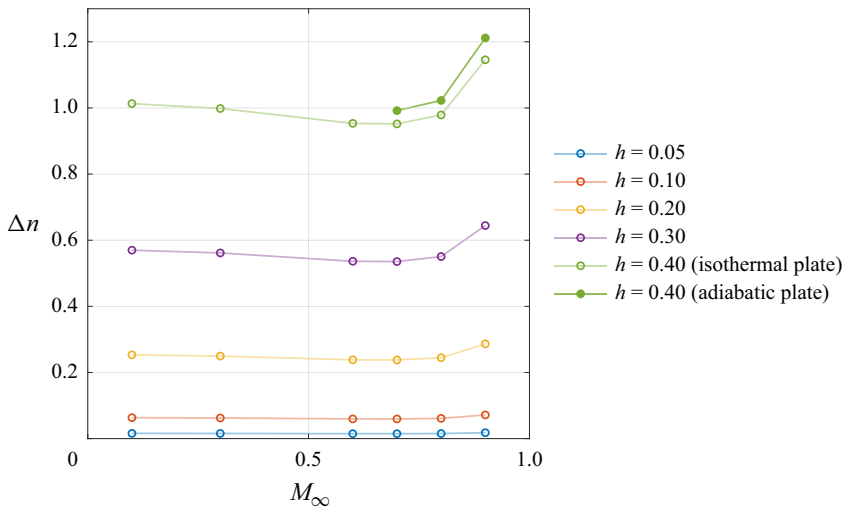

Figure 27. The Δn-factor caused by bumps of varying height vs the Mach number. For each M_∞, the TS wave is that which is dominant at $x = 500.0$ considering the smooth case. Bumps at $Re_{\delta*} = 950$ ($x_R = 320.8$) with length $L = 18.2$.

this region does not significantly affect the overall impact of the bump on the TS wave evolution. Downstream of the bump, for $M_\infty = 0.8$ and especially for $M_\infty = 0.9$, the shape factor deviation extends over a longer region. The displacement thickness deviation also stretches further downstream with M_∞, while the momentum thickness deviation is less sensitive to M_∞.
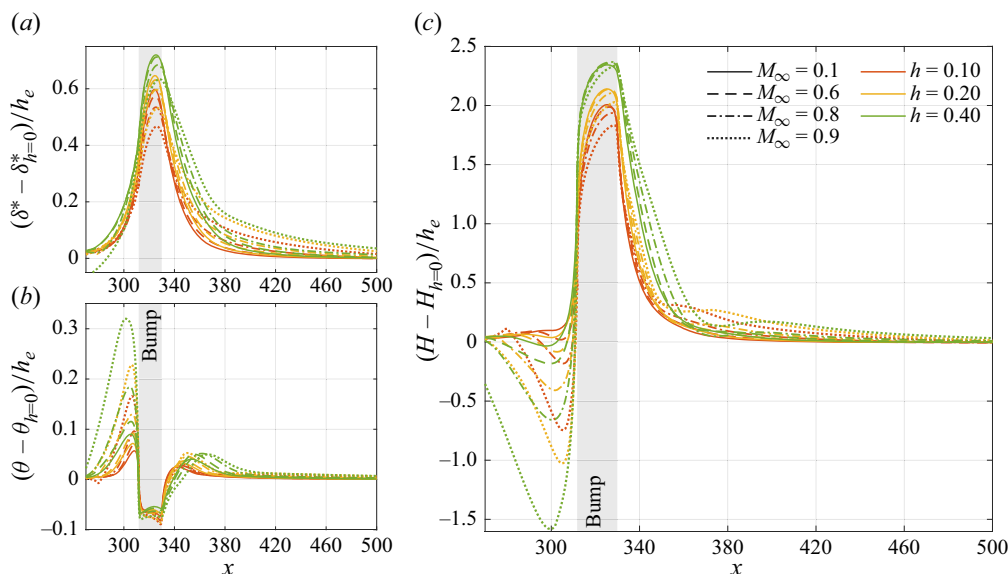
998 A11-30

Figure 28. Deviation caused by selected bumps relative to the smooth case in the distribution of the (*a*) displacement thickness, (*b*) momentum thickness and (*c*) shape factor. Results are normalised by the effective dimensionless bump height, $h_e = h/\delta^*_{h=0}(x_R)$. Bumps at $Re_{\delta^*} = 950$ ($x_R = 320.8$) with length $L = 18.2$.

The pressure distribution, C_p, is shown in figure 29(*a*). The values were taken at the iso-velocity curve of $u/U_\infty = 99\,\%$. The magnitude of the $C_{p_{u99}}$ distribution increases with Mach number but, on the bump's top, the curves collapse fairly well if the Prandtl–Glauert similarity rule is applied, figure 29(*b*). Recall that the Prandtl–Glauert rules depend on the aspect ratio of the body ($h^\star/L_R^\star$) and not on the boundary layer thickness. Downstream of the bump, the collapse is not as good. Clearly, the higher pressure gradients observed at higher Mach numbers retard the reattachment point. This is consistent with and potentialised by the longer tail of the boundary layer displacement thickness deviation (figure 28*a*) at the higher M_∞.

Figure 30(*a*) shows that the recirculation length ($L_{recirc.}$) correlates well with the value of $C_{p_{u99}}$ at the bump trailing edge. Figure 30(*b*) shows that, even though the pressure distribution does not conform to the Prandtl–Glauert rule along the bump wake (figure 29*b*), $L_{recirc.}$ correlates very well with this similarity rule. The value of $L_{recirc.}$ is not significantly increased in the low-subsonic regime, but the figure suggests that it is likely to be massively larger in the transonic regime. Masad & Iyer (1994) had already pointed out that, below $M_\infty = 0.8$, the destabilising effect caused by the bump in the compressible scenario is connected with the length of the recirculation, but they indicated that this effect was smaller than the stabilising effect of M_∞ in the TS waves. Our results confirm this destabilising effect observed by Masad & Iyer (1994), but we found that it becomes dominant above $M_\infty = 0.7$. Our numerical procedures could not cope with the sonic flow, but the results in figure 27 suggest that, towards $M_\infty = 1.0$, there is a substantial increment in comparison with that at $M_\infty = 0.7$.

At transonic speeds, the flow in the boundary layer heats up considerably and the use of either isothermal or adiabatic walls needs to be considered (Mengaldo *et al.* 2015). For an adiabatic wall, the higher temperatures thickens the boundary layer and the issue of the effective non-dimensional bump height becomes more relevant. This is shown in figure 26,
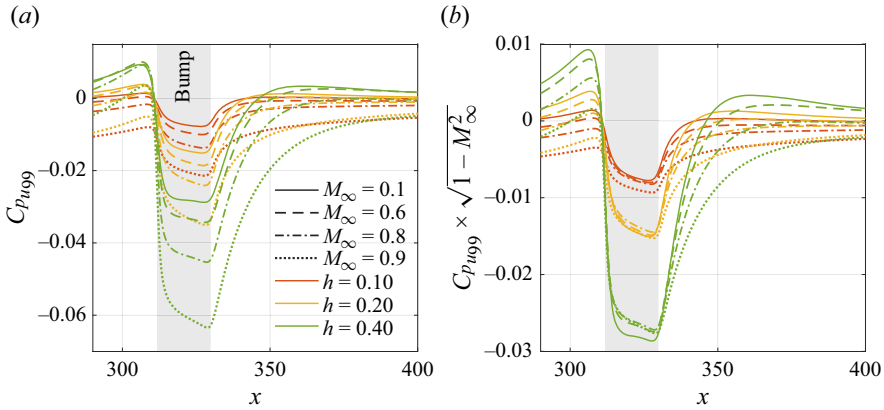
998 A11-31

Figure 29. (*a*) Distribution of pressure coefficient, C_p, along the iso-velocity curve where $u/U_\infty = 99\,\%$ for selected bump heights and Mach numbers. (*b*) Collapse of C_p curves by considering the Prandtl–Glauert similarity rule for compressible flows, $\sqrt{1 - M_\infty}$. Bumps at $Re_{\delta*} = 950$ ($x_R = 320.8$) with length $L = 18.2$.
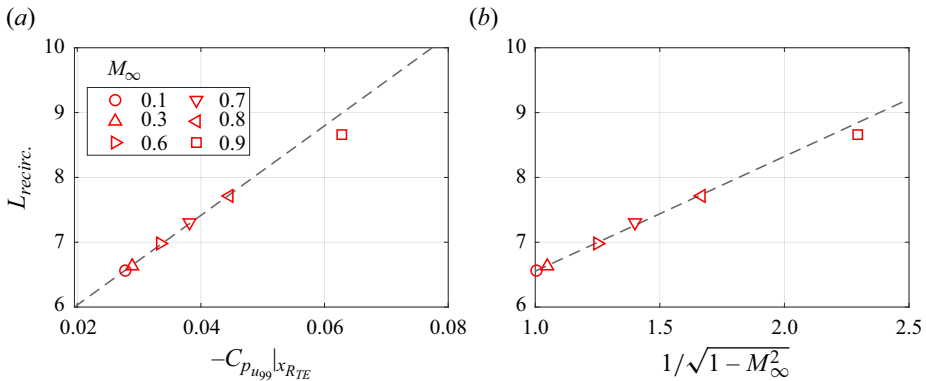

Figure 30. Length of the recirculating flow caused by the bump of $h = 0.40$ vs (*a*) $C_{p_{u99}}$ at the bump trailing edge and (*b*) considering the Prandtl–Glauert similarity rule.

where the curve for the adiabatic wall at $M_\infty = 0.9$ further diverges from those of lower M_∞. The results for the adiabatic wall, corrected via figure 26, are also plotted in 27. The adiabatic wall enhances the effect of the bump on the TS wave and the destabilising effect at transonic speeds. This is particularly relevant because this condition is likely to better represent that of cruise flight.

9. Conclusions

In this study, we aimed at investigating the effect of the Reynolds number on the interaction between bumps and TS waves. Early studies indicate an effect that has been overlooked in the more recent literature. We also investigated the effect of compressibility, in particular as it approaches the sonic speed. We used an in-house DNS code in the study. The bump was rectangular with sharp edges fitted to the grid. As the bump contains sharp corners immersed in the flow, they represent the most critical condition concerning its shape. The code produced very precise simulations that captured accurately even the effect of 2.5 %

on the amplitude of the TS wave caused by the very small bump with a height of 5 % of the local displacement thickness.

Within the bump wake, a recirculating flow region can be formed. The separation bubble length scales quadratically with bump height even for relatively small heights. Sufficiently far downstream, the boundary layer returns to that of the smooth plate, indicating the end of the so-called recovery zone. The profiles in the bump wake deviate from the Blasius one. The deviation scales linearly with height up to $h = 0.10$. Consistent with the base flow deviation, up to $h = 0.10$, the growth rate deviation scales linearly with bump height, which leads to an exponential variation of the amplification factor with respect to h. Above $h = 0.10$, the variation is super-exponential and the exponent can be well represented by a quadratic function of h. This quadratic–exponential function is associated with the strong influence of the bump height on the TS wave amplification reported in the literature.

In investigating the Reynolds number, we found that, under some circumstances, its effect can be substantial. First, there is an effect associated with the modification of the base flow. As the Reynolds number increases the magnitude of the wake profile deviation with respect to the smooth scenario also increases. The length of the wake extends with the Reynolds number as well. Both effects are destabilising. The effect of Reynolds number on the interaction between the TS wave and the bump could be encapsulated into a broader concept, which is the effect of bump proximity to the upper branch of the instability loop of the smooth plate. It turns out that the bump impact increases for TS waves that are closer to crossing the upper branch of the smooth plate instability loop. This amounts to an effect of TS wave frequency as well. The physical explanation stems from the fact that the bump wake profiles are distorted in a way that is similar to that caused by an adverse pressure gradient, which is known to enhance the instability mostly by raising the upper branch of the instability loop towards higher frequencies.

The effect of the upper branch dictates that the bump influence becomes more severe the closer it is to transition. As an example, changing the bump-location $Re_{\delta*}$ by a factor of 30 % can double the ΔN factor. The upper branch effect also implies that the TS wave–bump interaction becomes stronger as the transition moves upstream (decreasing N_{cr}), which could be caused by an increase in free-stream turbulence level, for example. In this situation, the TS wave frequency leading to transition would also increase, which means that the wave leading to transition interacted with the bump closer to its upper branch crossing. On the other hand, if the transition occurs far downstream of the bump, the TS wave leading to transition has a lower frequency and the interaction occurs farther from its upper branch crossing. The upper branch effect also shifts upwards the dominant TS wave frequency at each x-station, but this has a negligible impact on the calculations of ΔN.

The maximum impact exerted by a bump is related to the existence of a maximum ΔN value that occurs some distance downstream of the bump. For the sharp-edged rectangular bumps we investigated, $(\Delta N)_{max}$ scaled almost linearly with Re_{hh}. The length of the recirculating flow also conforms to a linear dependency on Re_{hh}. These results suggest that the maximum bump impact is associated with the recirculating flow in its wake.

With regard to M_∞, we confirmed that, up to a point, there is an overall stabilising effect on the TS wave despite the small increase of the recirculation length. For Mach numbers above 0.7, the recirculation region increases massively and the influence of M_∞ on the evolution of a TS wave over a bump becomes destabilising. Many features of the effect M_∞ can be well estimated by the Prandtl–Glauert similarity rule for compressible flows. The results suggest a significant impact in transonic regime. Considering adiabatic walls, instead of isothermal ones, leads to further destabilisation as we approach the transonic regime.

Declaration of interests. The authors report no conflict of interest.

Author ORCIDs.

Fernando H.T. Himeno https://orcid.org/0000-0002-2345-5628;

A.E.B. Carvalho https://orcid.org/0009-0000-1433-9409;

M.A.F. Medeiros https://orcid.org/0000-0003-4174-6258.

REFERENCES

ÅKERVIK, E., BRANDT, L., HENNINGSON, D.S., HŒPFFNER, J., MARXEN, O. & SCHLATTER, P. 2006 Steady solutions of the Navier–Stokes equations by selective frequency damping. *Phys. Fluids* **18** (6), 068102.

BERGAMO, L.F., GENNARO, E.M., THEOFILIS, V. & MEDEIROS, M.A.F. 2015 Compressible modes in a square lid-driven cavity. *Aerosp. Sci. Technol.* **44**, 125–134.

CARMICHAEL, B.H. 1959 Surface waviness criteria for swept and unswept laminar suction wings. In *Norair Rep.*, *BLC-123* NOR-59-438. Northrop Corp.

CEBECI, T. & EGAN, D.A. 1989 Prediction of transition due to isolated roughness. *AIAA J.* **27** (7), 870–875.

COSTANTINI, M., RISIUS, S. & KLEIN, C. 2022 Step-induced transition in compressible high Reynolds number flow. *Flow* **2**, E33.

CROUCH, J.D. & KOSORYGIN, V.S. 2020 Surface step effects on boundary-layer transition dominated by Tollmien–Schlichting instability. *AIAA J.* **58** (7), 2943–2950.

CROUCH, J.D., KOSORYGIN, V.S. & NG, L.L. 2006 Modeling the effects of steps on boundary-layer transition. In *IUTAM Symp. on Laminar-Turbulent Transition* (ed. R. Govindarajan), Fluid Mech. Appl., vol. 78, pp. 37–44. Springer.

DOVGAL, A.V. & KOZLOV, V.V. 1990 Hydrodynamic instability and receptivity of small scale separation regions. In *IUTAM Symp. on Laminar-Turbulent Transition* (ed. D. Arnal & R. Michel), pp. 523–531. Springer.

DRYDEN, H.L. 1953 Review of published data on the effect of roughness on transition from laminar to turbulent flow. *J. Aeronaut. Sci.* **20** (7), 477–482.

FAGE, A. & PRESTON, J.H. 1941 On transition from laminar to turbulent flow in the boundary layer. *Proc. R. Soc. Lond.* A **178** (973), 201–227.

GAITONDE, D. & SHANG, J. 1996 High-order finite-volume schemes in wave propagation phenomena. *AIAA Paper* 93-2335.

GAITONDE, D. & VISBAL, M.R. 1998 High-order schemes for Navier–Stokes equations: algorithm and implementation into FDL3DI. *Tech. Rep.* AFRL-VA-WP-TR-1998-3060. Air Force Research Laboratory, Wright-Patterson AFB, OH.

HILDEBRAND, N., CHOUDHARI, M.M. & PAREDES, P. 2020 Predicting boundary-layer transition over backward-facing steps via Linear Stability Analysis. *AIAA J.* **58** (9), 3728–3734.

HIMENO, F.H.T., CARVALHO, A.E.B. & MEDEIROS, M.A.F. 2023 Effect of small rectangular bumps on the amplification of Tollmien–Schlichting waves. *AIAA Paper* 2023-3996.

HIMENO, F.H.T., MATHIAS, M.S. & MEDEIROS, M.A.F. 2021 DNS of a Tollmien–Schlichting wave interacting with a roughness modeled via body-fitted and approximation methods. *AIAA Paper* 2021-2500.

VAN INGEN, J.L. 1956 A suggested semi-empirical method for the calculation of the boundary layer transition region. *Tech. Rep.* Report UTH1-74. Univ. of Tech., Delft, Nederlands.

JUNIPER, M.P., HANIFI, A. & THEOFILIS, V. 2014 Modal stability theory. In *Lecture notes FLOW-NORDITA Summer School on Advanced Instability Methods for Complex Flows*, vol. 66, p. 021004. Appl. Mech. Rev.

KACHANOV, Y.S. 1994 Physical mechanisms of laminar-boundary-layer transition. *Annu. Rev. Fluid Mech.* **26** (1), 411–482.

KLEBANOFF, P.S. & TIDSTROM, K.D. 1972 Mechanism by which a two-dimensional roughness element induces boundary-layer transition. *Phys. Fluids* **15** (7), 1173–1188.

LELE, S.K. 1992 Compact finite difference schemes with spectral-like resolution. *J. Comput. Phys.* **103** (1), 16–42.

LI, N. & LAIZET, S. 2010 2DECOMP & FFT – a highly scalable 2D decomposition library and FFT interface. In *Proc. of the Cray User Group 2010*, pp. 1–13. Cray User Group.

MAREC, J.P. 2001 Drag reduction: a major task for research. In *Aerodynamic Drag Reduction Technologies Proceedings of the CEAS/DragNet European Drag Reduction Conference* (ed. P. Thiede), pp. 17–27. Springer.

MARTINEZ, A.G. & MEDEIROS, M.A.F. 2016 Direct Numerical Simulation of a wavepacket in a boundary layer at Mach 0.9. *AIAA Paper* 2016-3195.

MASAD, J.A. & IYER, V. 1994 Transition prediction and control in subsonic flow over a hump. *Phys. Fluids* **6** (1), 313–327.

MATHIAS, M.S. & MEDEIROS, M.A.F. 2018 Direct Numerical Simulation of a compressible flow and matrix-free analysis of its instabilities over an open cavity. *J. Aerosp. Technol. Manage.* **10**, e3718.

MATHIAS, M.S. & MEDEIROS, M.A.F. 2021 The effect of incoming boundary layer thickness and mach number on linear and nonlinear rossiter modes in open cavity flows. *Theor. Comput. Fluid Dyn.* **35** (4), 495–513.

MEDEIROS, M.A.F. & GASTER, M. 1999*a* The influence of phase on the nonlinear evolution of wavepackets in boundary layers. *J. Fluid Mech.* **397**, 259–283.

MEDEIROS, M.A.F. & GASTER, M. 1999*b* The production of sub-harmonic waves in the nonlinear evolution of wavepackets in boundary layers. *J. Fluid Mech.* **399**, 301–318.

MENGALDO, G., KRAVTSOVA, M., RUBAN, A.I. & SHERWIN, S.J. 2015 Triple-deck and direct numerical simulation analyses of high-speed subsonic flows past a roughness element. *J. Fluid Mech.* **774**, 311–323.

MORKOVIN, M.V. 1969 On the many faces of transition. In *Viscous Drag Reduction* (ed. C.S. Wells), pp. 1–31. Springer.

MORKOVIN, M.V. 1990 On roughness–induced transition: facts, views, and speculations. In *Instability and Transition* (ed. M.Y. Hussaini & R.G. Voigt), pp. 281–295. Springer.

NAYFEH, A.H. 1992 Influence of two-dimensional imperfections on laminar flow. *Tech. Rep.* SAE Tech. Paper.

NAYFEH, A.H., RAGAB, S.A. & AL-MAAITAH, A.A. 1988 Effect of bulges on the stability of boundary layers. *Phys. Fluids* **31** (4), 796–806.

OBARA, C.J. & HOLMES, B.J. 1986 Roughness and waviness requirements for laminar flow surfaces. In *Langley Symp. on Aerodyn.*, vol. 1, pp. 519–538. NASA Langley Research Center.

DE PAULA, I.B., WÜRZ, W. & MEDEIROS, M.A.F. 2008 Experimental study of a Tollmien–Schlichting wave interacting with a shallow 3d roughness element. *J. Turbul.* **9**, N7.

DE PAULA, I.B., WÜRZ, W., MENDONÇA, M.T. & MEDEIROS, M.A.F. 2017 Interaction of instability waves and a three-dimensional roughness element in a boundary layer. *J. Fluid Mech.* **824**, 624–660.

PERRAUD, J., ARNAL, D., SERAUDIE, A. & TRAN, D. 2004 Laminar-turbulent transition on aerodynamic surfaces with imperfections. In *Proc. RTO AVT-111 Symp.* NATO.

PLACIDI, M., GASTER, M. & ATKIN, C.J. 2020 Acoustic excitation of Tollmien–Schlichting waves due to localised surface roughness. *J. Fluid Mech.* **895**, 1–13.

RAPOSO, H., MUGHAL, S.M. & ASHWORTH, R. 2018 Acoustic receptivity and transition modeling of Tollmien–Schlichting disturbances induced by distributed surface roughness. *Phys. Fluids* **30** (4), 044105.

RESHOTKO, E. 1976 Boundary-layer stability and transition. *Annu. Rev. Fluid Mech.* **8** (1), 311–349.

DOS SANTOS, P.H.R., HIMENO, F.H.T., MATHIAS, M.S. & MEDEIROS, M.A.F. 2024 Physical aspects of Tollmien–Schlichting wave acoustic receptivity due to sharp-edged rectangular bumps and gaps investigated via subsonic high-fidelity simulations. *J. Fluid Mech.* (submitted).

SARIC, W.S., REED, H.L. & KERSCHEN, E.J. 2002 Boundary-layer receptivity to freestream disturbances. *Annu. Rev. Fluid Mech.* **34** (1), 291–319.

SCHLICHTING, H. & GERSTEN, K. 2000 *Boundary Layer Theory*, 8th edn. Springer.

SILVA, H.G., SOUZA, L.F. & MEDEIROS, M.A.F. 2010 Verification of a mixed high-order accurate DNS code for laminar turbulent transition by the method of manufactured solutions. *Intl J. Numer. Meth. Fluids* **64** (3), 336–354.

SMITH, A.M.O. & GAMBERONI, N. 1956 Transition, pressure gradient and stability theory. *Tech. Rep.* ES26388. Douglas Aircraft Co.

SUMARIVA, J.A.F., HEIN, S. & VALERO, E. 2020 On the influence of two-dimensional hump roughness on laminar-turbulent transition. *Phys. Fluids* **32** (3), 034102.

TANI, I. 1961 Effect of two-dimensional and isolated roughness on laminar flow. In *Boundary Layer and Flow Control* (ed. G.V. Lachmann), pp. 637–656. Pergamon.

TANI, I., HAMA, R. & MITUISI, S. 1940 On the permissible roughness in the laminar boundary layer. *Rep. Aeronaut. Res. Inst. Tokyo Univ.* **15** (199), 417–428.

THOMAS, C., MUGHAL, S.M. & ASHWORTH, R. 2017 Development of Tollmien–Schlichting disturbances in the presence of laminar separation bubbles on an unswept infinite wavy wing. *Phys. Rev. Fluids* **2**, 043903.

THOMAS, C., MUGHAL, S.M., ROLAND, H., ASHWORTH, R. & MARTINEZ-CAVA, A. 2018 Effect of small surface deformations on the stability of Tollmien–Schlichting disturbances. *AIAA J.* **56** (6), 2157–2165.

WANG, Y.X. & GASTER, M. 2005 Effect of surface steps on boundary layer transition. *Exp. Fluids* **39** (4), 679–686.

WIE, Y.S. & MALIK, M.R. 1998 Effect of surface waviness on boundary-layer transition in two-dimensional flow. *Comput. Fluids* **27** (2), 157–181.

WÖRNER, A., RIST, U. & WAGNER, S. 2003 Humps/steps influence on stability characteristics of two-dimensional laminar boundary layer. *AIAA J.* **41** (2), 192–197.

XU, H., MUGHAL, S.M., GOWREE, E.R., ATKIN, C.J. & SHERWIN, S.J; 2017 Destabilisation and modification of Tollmien–Schlichting disturbances by a three-dimensional surface indentation. *J. Fluid Mech.* **819**, 592–620.